Journal of Computational Physics 433 (2021) 110178

Contents lists available at ScienceDirect

Journal of Computational Physics

www.elsevier.com/locate/jcp

A new coupled multiphase flow–finite strain deformation–fault slip framework for induced seismicity

Xiaoxi Zhao, Birendra Jha *

Mork Family Department of Chemical Engineering and Materials Science, University of Southern California, Los Angeles, CA, USA

ARTICLE INFO

Article history:
Available online 8 February 2021

Keywords:
Finite strain
Poroplasticity
Multiphase flow
Geomechanics
Induced seismicity

ABSTRACT

Production of hydrocarbons and water from subsurface reservoirs are known to cause permanent deformation of the reservoir and seismicity along faults both of which are detrimental to sustainable development of natural resources. Most of the prior studies on understanding fluid flow-induced plasticity and seismicity have focused on one or the other phenomenon due to the numerical difficulty associated with simultaneous modeling of the two failure phenomena because stress and deformation evolve non-linearly in both plasticity and seismicity. However, in reservoirs undergoing long-term production, plastic failure can alter the stress paths of points on a fault such that the onset, location, and magnitude of actual seismic events can no longer be predicted by a poroelastic simulation due to inaccurate stress and deformation history. We present a computational framework for coupled multiphase flow, finite strain poroplastic deformation, and dynamic fault slip and use it to understand the impact of plastic deformation on the onset, location, and magnitude of induced fault slip events. We evaluate the impact of plasticity on reservoir pressure, deformation, induced stress, and fault slip by comparing infinitesimal strain elastic and finite strain poro-elastoplastic models. For real-world applications, we consider different scenarios where the reservoir is either mechanically weaker or stronger than the caprock. We analyze the stress evolution as a function of the change in reservoir pressure to understand the role of contrast in reservoir and caprock elastic moduli on geomechanical stability. The results show that the poroplastic reservoir exhibits larger vertical deformation and delayed slip than the poroelastic reservoir after the same amount of oil production. For the same amount of pressure drop, a reservoir with a smaller modulus than the caprock displays a larger vertical displacement and an earlier onset of both plastic failure and fault slip. For a reservoir with a larger modulus than the caprock, vertical displacement is larger on the reservoir top boundary and smaller on the ground surface, and a higher pressure drop is needed to induce plastic failure and fault slip.

1. Introduction

Production and injection activities in faulted and stress-sensitive reservoirs can raise concerns of fault destabilization [1–3]. Coupled numerical modeling of fluid flow and mechanical deformation in such reservoirs is an active area of research for the purpose of assessing the hazards of fault reactivation and induced seismicity during oil production [4–8],

* Corresponding author.
E-mail address: bjha@usc.edu (B. Jha).

https://doi.org/10.1016/j.jcp.2021.110178
0021-9991/

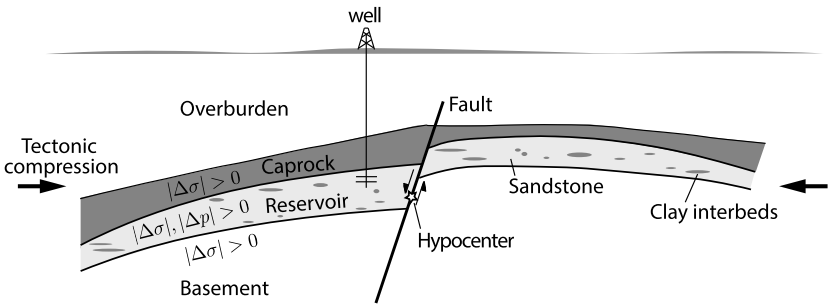

Fig. 1. Model problem of flow-induced deformation in a faulted reservoir-caprock system. Well operation causes a change in the pore pressure ($|\Delta p| > 0$) and a change in the state of stress ($|\Delta\sigma| > 0$) inside the permeable reservoir and a change in the state of stress in caprock and basement. If the stress change is large enough, it can induce plastic/permanent deformation in the rock. If the fault is critically-stressed (depends on fault's dip, cohesion and friction, and tectonic compression), the stress change can induce fault slip at the hypocenter.

gas production [9,10], water extraction [11], wastewater disposal [12–14], geologic CO_2 sequestration [15–17], and hydraulic fracturing [18]. However, most of these studies assume a linear elastic infinitesimal deformation response of the rock hosting the fault. We know that deformation response of many rocks, such as clayey sands, ultra-low permeability shales, and carbonates can become viscoelastic or elstoplastic at large effective stresses typically encountered during long-term production or injection [19–21]. Hard brittle rocks also show inelastic stress-strain behaviors through microcracking activity [22]. Long-term groundwater withdrawal in California's Central Valley [23,24] and oil and water production in Wilmington [25,26] and Gulf of Mexico [7] oilfields are examples where both large strains (e.g., $> 2\%$) and plastic deformation are expected to occur. Plastic deformation also occurs at relatively small values of the induced stresses if the rock is mechanically weak or ductile, e.g. chalk reservoirs in Ekofisk [27], some shales [28,29], and clay beds or aquitards [30]. Presence of clay particles or interbeds in sandstone aquifers can give rise to a lag in the mechanical response of aquifers under depletion [31,32], which manifests as plasticity. In general, long-term fluid extraction or injection activities can activate nonlinearity in both the material constitutive response and the kinematics of deformation. Use of elastic and infinitesimal deformation models in those cases will predict inaccurate stresses and, therefore, inaccurate onset, magnitude, and duration of the fault slip events. This is especially problematic for smaller magnitude earthquakes or aseismic slip events (Mw$<$4), which are not felt by humans but may cause damage to surface facilities and leakage of reservoir fluids (or other types of stored fluids such as natural gas or CO_2) along the activated fault into freshwater resources. Other manifestations of plastic deformation include drop in the reservoir permeability, loss of well productivity/injectivity, and wellbore failure [25,33].

Once a rock fails plastically, its stress path can deviate significantly from that of an elastically deforming rock in reservoirs that are producing or injecting for decades. Plastic dissipation also changes the mechanical energy budget such that energy available for brittle shear or tensile failure events can be expected to be smaller [34]. Given that fault slip is an irreversible deformation process, and it is coupled to stresses in the host rock and driven by the elastic strain energy accumulated during production/injection, we hypothesize that the changes induced by plasticity in the stress path of the host rock can change the onset, location, magnitude and duration of the induced slip events. The present study tests this hypothesis.

Accounting for the above changes can improve the agreement between model-predicted seismicity and ground deformation [11,35] and the observed data. Therefore, there is an urgent need to develop simulation methods that resolve coupled flow, geomechanics, and dynamic faulting processes in plastically deforming rocks and demonstrate their application to real reservoirs. Over the years, multiple coupled flow and elastoplastic geomechanical frameworks have been proposed [36–47], mostly in absence of fault slip. Here, we build on that foundation to develop such a method. Applying the method to faulted reservoir-caprock systems with realistic geological structure, heterogeneous rock properties, and multiphase flow is another challenge that we tackle. The paper is organized as follows. First, we present the mathematical problem of coupled multiphase flow, finite strain plasticity, and dynamic fault slip. The numerical model based on a finite element discretization of the mechanics problem and a finite volume discretization of the flow problem is presented next. The model is tested on benchmark consolidation problems before being applied to a realistic case of oil production from an anticlinal oil reservoir confined by caprock and basement and intersected by a fault. Results from simulations with different elastic moduli for reservoir and caprock layers are analyzed to understand the impact of plasticity on characteristics of fault slip in different rock types.

2. Coupled multiphase flow, finite strain poromechanics, and fault slip

Consider the deformation of an oil reservoir, confined between caprock and basement and intersected by a fault, due to oil production from a well drilled into the reservoir. See Fig. 1 for a schematic of the conceptual problem. The porous medium has three phases: the solid skeleton, which is made up of solid grains and pores, and the two fluid phases that occupy the pores [48]. Now, let's consider the deformation of a representative elementary volume (REV) $V^0 \subset \mathbb{R}^3$ of the reservoir (Fig. 2). Γ^0 is the boundary of the REV. We denote the reference configuration of the volume by the solid particle position vector $\boldsymbol{X} \in \mathbb{R}^3$ and the fluid particle position vectors $\boldsymbol{X}_o$ and $\boldsymbol{X}_w$, where subscripts o and w refer to oil and

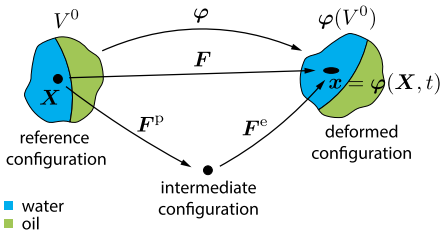

Fig. 2. Kinematics of a porous body saturated with two fluids. $\boldsymbol{\varphi}$ is the solid deformation mapping. Mappings of the two fluid phases are not shown for brevity. Multiplicative elastoplasticity is implied by the decomposition of the deformation gradient $\boldsymbol{F}$ into elastic $\boldsymbol{F}^{\mathrm{e}}$ and plastic $\boldsymbol{F}^{\mathrm{p}}$ parts and the stress-free intermediate configuration.

water phases. Let $\boldsymbol{\varphi} : V^0 \times [0, t] \to \mathbb{R}^3$ be the solid deformation mapping, where t denotes time. After deformation, the current or deformed configuration is given by the position vector $\boldsymbol{x}$, which is occupied by all three phases simultaneously. The deformed volume is V within the boundary Γ. The solid phase deformation vector is $\boldsymbol{u} = \boldsymbol{x} - \boldsymbol{X}$, and the solid phase deformation gradient tensor is $\boldsymbol{F} = \nabla_X \boldsymbol{x} = \mathbf{1} + \nabla_X \boldsymbol{u}$, where ∇_X denotes partial derivatives with respect to $\boldsymbol{X}$ and $\mathbf{1}$ is the rank-2 identity tensor. We will use $\nabla = \boldsymbol{F}^{-\mathrm{T}} \nabla_X$ to denote partial derivatives with respect to current coordinates $\boldsymbol{x}$. The superscript $^{-\mathrm{T}}$ indicates transpose of inverse. Let $M = M_w + M_o$ be the total fluid mass in the reference configuration per unit bulk volume in the reference configuration, where $M_w = \rho_w \phi s_w J$ is the water mass content, $M_o = \rho_o \phi s_o J$ is the oil mass content, ϕ is the true or Eulerian porosity defined as the pore volume in the current configuration over the bulk volume in the current configuration, ρ_w and ρ_o are water and oil densities in the current configuration, s_w and s_o are water and oil saturations in the current configuration with respect to the current pore volume, and $J = \det \boldsymbol{F} = dV/dV^0$ is the Jacobian of solid deformation. The saturations must sum to 1 by definition: $s_w + s_o = 1$. The Lagrangian porosity (current pore volume per unit reference bulk volume) is defined as $\Phi = \phi J$. As commonly considered in the literature [39], we take the solid motion as the reference motion and describe the fluid motion relative to the solid motion.

We have the following strain and deformation tensors:

$$\boldsymbol{E} = (1/2)(\boldsymbol{F}^{\mathrm{T}} \boldsymbol{F} - \mathbf{1}) = (1/2)\left(\nabla_X \boldsymbol{u} + \boldsymbol{u} \nabla_X + \nabla_X \boldsymbol{u} \cdot \boldsymbol{u} \nabla_X\right), \tag{1}$$

$$\boldsymbol{\varepsilon} = (1/2)\left(\nabla \boldsymbol{u} + \boldsymbol{u} \nabla\right) = \mathrm{sym}[\nabla \boldsymbol{u}], \tag{2}$$

$$\boldsymbol{b} = \boldsymbol{F} \boldsymbol{F}^{\mathrm{T}}, \tag{3}$$

$$\boldsymbol{C} = \boldsymbol{F}^{\mathrm{T}} \boldsymbol{F} \tag{4}$$

where $\boldsymbol{E}$ is the Green-Lagrange strain tensor, $\boldsymbol{\varepsilon}$ is the infinitesimal strain tensor, $\boldsymbol{b}$ is the left Cauchy-Green deformation tensor and $\boldsymbol{C}$ is the right Cauchy-Green deformation tensor. Here, sym denotes the symmetric operator. The linearized volumetric strain in the current configuration is $\varepsilon_v = \mathrm{tr}[\boldsymbol{\varepsilon}] = \log J$. This yields $J = \exp(\varepsilon_v)$, which is approximated as $J = 1 + \varepsilon_v$ in the infinitesimal deformation theory. As fluid is produced from or injected into the reservoir, principles of conservation of mass and momentum of the solid and fluid components govern the evolution of state variables of the system such as stress, strain, fluid mass content, and fluid pressure.

2.1. Balance laws

Mass conservation We assume quasi-static mechanical equilibrium. The mass content of the solid phase is conserved. This will be utilized later to obtain the porosity evolution equation. The conservation equation of the water phase mass during deformation, written in the reference configuration of the porous medium, reads as

$$\dot{M}_w + J \nabla \cdot \boldsymbol{w}_w + J q_w = 0, \quad \text{in} \quad V^0 \tag{5}$$

where $\dot{(\,)}$ denotes the material time derivative, $\boldsymbol{w}_w = \rho_w \boldsymbol{v}_w$ is the water mass flux, q_w is the water mass production term due to wells, $\boldsymbol{v}_w = -(\boldsymbol{k} k_{rw}/\mu_w) \cdot (\nabla p_w - \rho_w \boldsymbol{g})$ is the water volumetric flux or the Darcy velocity (obtained from the conservation of fluid momentum after neglecting inertia, drag, and viscous forces), p_w is the excess water pressure (above the initial pore pressure), $\boldsymbol{k}$ is the rank-2 permeability tensor, μ_w is the dynamic viscosity of the water, k_{rw} is the relative permeability of water in presence of oil, and $\boldsymbol{g}$ is the acceleration vector due to gravity. The flux terms are in the current configuration. The permeability transforms as $\boldsymbol{k} = (1/J) \boldsymbol{F} \boldsymbol{k}^0 \boldsymbol{F}^{\mathrm{T}}$, where $\boldsymbol{k}^0$ is the permeability tensor in the reference configuration. The water mass content in the current configuration is $m_w = M_w / J$. By definition, the water density in the reference configuration is $\rho_w^0 = J \rho_w$. Similar to Eq. (5), we have another conservation equation for the oil phase mass M_o that introduces the Darcy flux of oil in terms of ρ_o, oil viscosity μ_o, oil relative permeability k_{ro}, and oil phase pressure p_o. Since oil and water are immiscible phases, the difference between their pressures is the capillary pressure $P_c = p_o - p_w$, which is often modeled via a saturation-dependent capillary pressure relation, also known as the retention curve in air-water systems studied in soil hydrology. A non-zero capillary pressure can affect the elastic stiffness of the porous medium.

Momentum conservation Given the possibility of large deformations and rotations in the finite strain theory, and the need to track the displacement of the solid skeleton from its reference configuration, it is customary to write the conservation of linear momentum in the reference configuration as

$$\nabla_X \cdot \boldsymbol{P} + J\rho_b \boldsymbol{g} = \boldsymbol{0}, \quad \forall \boldsymbol{X} \in V^0 \tag{6}$$

where $\boldsymbol{P} = J\boldsymbol{\sigma}\boldsymbol{F}^{-T}$ is the first Piola-Kirchhoff (PK) stress tensor (asymmetric tensor) defined in terms of the total Cauchy stress tensor $\boldsymbol{\sigma}$ (symmetric). $\boldsymbol{\sigma}$ is a measure of force acting on an area in the current configuration per unit area in the current configuration. $\boldsymbol{P}$ is a measure of force acting on an area in the current configuration per unit area in the reference configuration. Above, $\rho_b = (1-\phi)\rho_s + \phi(\rho_o s_o + \rho_w s_w)$ is the bulk density in the current configuration, and ρ_s is the solid grain density. The second PK stress tensor, which measures force in the reference configuration per unit area in the reference configuration (symmetric tensor), is defined as $\boldsymbol{S} = J\boldsymbol{F}^{-1}\boldsymbol{\sigma}\boldsymbol{F}^{-T}$, which shows how the stress in the current configuration can be pulled back to the reference configuration. This also implies $\boldsymbol{P} = \boldsymbol{F}\boldsymbol{S}$. When $\boldsymbol{F} \simeq \boldsymbol{1}$ and $J \simeq 1$, $\boldsymbol{S}$ can be replaced by $\boldsymbol{\sigma}$, and $\boldsymbol{E}$ can be replaced by $\boldsymbol{\varepsilon}$ such that we recover the infinitesimal strain model. The Kirchhoff stress tensor in the current configuration is defined as $\boldsymbol{\tau} = J\boldsymbol{\sigma} = \boldsymbol{F}\boldsymbol{S}\boldsymbol{F}^{\mathrm{T}}$. To facilitate constitutive modeling of fluid-saturated rocks, which is discussed in detail below, we define the effective stresses: the effective Kirchhoff stress $\boldsymbol{\tau}' = J\boldsymbol{\sigma}'$ and the effective second PK stress $\boldsymbol{S}' = J\boldsymbol{F}^{-1}\boldsymbol{\sigma}'\boldsymbol{F}^{-T}$.

2.2. Poroplastic deformation

Following the poroelastoplastic formulation proposed earlier [49,37,38], we use a multiplicative decomposition of $\boldsymbol{F}$ and an additive decomposition of total fluid mass M into their elastic and plastic parts:

$$\boldsymbol{F} = \boldsymbol{F}^{\mathrm{e}}\boldsymbol{F}^{\mathrm{p}}, \quad M = M^{\mathrm{e}} + M^{\mathrm{p}}, \tag{7}$$

where the superscripts $^{\mathrm{e}}$ and $^{\mathrm{p}}$ denote elastic and plastic parts, respectively. The elastic part of left Cauchy-Green tensor is $\boldsymbol{b}^{\mathrm{e}} = \boldsymbol{F}^{\mathrm{e}}\boldsymbol{F}^{\mathrm{e,T}}$. The elastic part of the right Cauchy-Green tensor is $\boldsymbol{C}^{\mathrm{e}} = \boldsymbol{F}^{\mathrm{e,T}}\boldsymbol{F}^{\mathrm{e}}$ and the plastic part is $\boldsymbol{C}^{\mathrm{p}} = \boldsymbol{F}^{\mathrm{p,T}}\boldsymbol{F}^{\mathrm{p}}$. The volumetric plastic strain $\varepsilon_v^{\mathrm{p}} = \varepsilon_v - \varepsilon_v^{\mathrm{e}} = \log J^{\mathrm{p}}$ with $J^{\mathrm{p}} = \det \boldsymbol{F}^{\mathrm{p}}$. For isochoric plastic flow, a common assumption in plasticity, $J^{\mathrm{p}} = 1$ and $J = \det \boldsymbol{F}^{\mathrm{e}}$.

2.3. Fault slip problem

To model seismic/aseismic slip on the fault, we treat the fault as a strong discontinuity, i.e. the displacement field is discontinuous across the fault, as opposed to the weak discontinuity which implies only a discontinuous strain field. The case of a strong discontinuity emerging inside an initially continuous finite element has been treated in the finite strain theory [50,44] by enhancing the deformation gradient in the nonconforming elements with an additional component related to the displacement jump and enhancing the finite element test functions with a Heaviside function. Here, we consider the conforming case where the fault slip is constrained to lie along the edges between adjacent finite elements. The conforming case is practical in many geological settings where geometry of the rupture surface of a seismogenic fault is known from previous earthquakes, well logs, or basin modeling studies. The approach requires construction of a mesh conforming to the fault geometry, which can be time-consuming in a 3D domain containing multiple intersecting or curved faults. However, simulation of the conforming case is expected to be faster than that of the nonconforming case which has to solve for the rupture path as well. We treat the fault as a frictional interface Γ_f (reference configuration) across which the displacement field can be discontinuous to accommodate seismic/aseismic slip. We define the fault slip vector $\boldsymbol{d}_f$ in the current configuration as the displacement discontinuity or jump from the '$-$' side (Γ_+) to the '$+$' side (Γ_-) of the fault (e.g. the footwall and hanging wall sides of a dip-slip fault) as

$$\boldsymbol{u}^+ - \boldsymbol{u}^- = \boldsymbol{d}_f \quad \text{on} \quad \Gamma_f. \tag{8}$$

We define $\hat{\boldsymbol{n}}_f$ as the unit normal vector on the fault (reference configuration) pointing from the -ve side to +ve side. The normal vector can vary in space for a fault that is either naturally arcuate or becomes curved due to reservoir expansion or contraction induced by fluid injection or production. Mechanical equilibrium requires continuity of the total traction vector across the fault: $\boldsymbol{T}_f^+ = (\boldsymbol{F}\boldsymbol{S})^+\hat{\boldsymbol{n}}_f = (\boldsymbol{F}\boldsymbol{S})^-\hat{\boldsymbol{n}}_f = \boldsymbol{T}_f^-$. The effective fault traction vector is a projection of the effective second PK tensor stress tensor on the fault: $\boldsymbol{l}_f = \boldsymbol{F}\boldsymbol{S}'\hat{\boldsymbol{n}}_f$. We define the local fault coordinate system using three mutually orthogonal unit vectors, $(\hat{\boldsymbol{s}}_1, \hat{\boldsymbol{s}}_2, \hat{\boldsymbol{n}}_f)$, which are positive in the left-lateral, updip and opening directions of the fault. $\boldsymbol{l}_f$ can be split into a shear traction vector and a normal traction vector as $(\boldsymbol{\tau}_s, \sigma_n'\hat{\boldsymbol{n}}_f)$ where $\boldsymbol{\tau}_s = (\boldsymbol{l}_f \cdot \hat{\boldsymbol{s}}_1)\hat{\boldsymbol{s}}_1 + (\boldsymbol{l}_f \cdot \hat{\boldsymbol{s}}_2)\hat{\boldsymbol{s}}_2$ lies on the 2D fault surface and $\sigma_n' = \boldsymbol{l}_f \cdot \hat{\boldsymbol{n}}_f$. Similarly, $\boldsymbol{d}_f$ can be split into the slip vector $\boldsymbol{d}_s = (\boldsymbol{d}_f \cdot \hat{\boldsymbol{s}}_1)\hat{\boldsymbol{s}}_1 + (\boldsymbol{d}_f \cdot \hat{\boldsymbol{s}}_2)\hat{\boldsymbol{s}}_2$, which points in the rake direction, and the fault opening d_n. Dual-porosity or dual-permeability aspects are not considered because the fault remains closed, and fluid is not allowed to flow within the fault during the period of analysis. Also, this study focuses on a reservoir scale analysis and the local fluid flux jump across the fault is ignored.

2.4. Constitutive relations

Minimization of the free energy of a system, as the system evolves dynamically, is often used to extract the constitutive relations applicable to the system. Let ψ be the free energy (per unit reference volume) of the elastoplastic system defined in terms of three internal variables: $\boldsymbol{b}^{\mathrm{e}}$, M^{e}, and a strain-like internal variable ξ which tracks the isotropic hardening response during plastic deformation. The rate of change of free energy can be written in terms of the stress power ($\boldsymbol{\tau} : \boldsymbol{d}$, $\boldsymbol{S} : \dot{\boldsymbol{E}}$, or $\boldsymbol{P} : \dot{\boldsymbol{F}}$), the fluid accumulation power, the power of faulting produced by the fault traction vector in realizing the slip across the fault, and the internal dissipation:

$$\int_{V^0} \dot{\psi} dV^0 = \int_{V^0} \left(\boldsymbol{\tau} : \boldsymbol{d} + \chi_w \dot{M}_w + \chi_o \dot{M}_o - \mathcal{D} \right) dV^0 + \int_{\Gamma_f^0} \boldsymbol{T}_f \cdot \dot{\boldsymbol{d}}_f \, d\Gamma^0 \tag{9}$$

where $\mathcal{D} = \boldsymbol{C}^{\mathrm{e}} \boldsymbol{S} : \boldsymbol{L}^{\mathrm{p}} + h\dot{\xi} + \chi_w \dot{M}_w^{\mathrm{p}} + \chi_o \dot{M}_o^{\mathrm{p}} - P_c \Phi \dot{s}_w \geq 0$ is the local internal dissipation (per unit reference volume) due to incremental plastic deformation, hardening, plastic fluid content, and capillarity (due to the surface energy associated with fluid interfaces in a multiphase system). Here, $\boldsymbol{L}^{\mathrm{p}} = \dot{\boldsymbol{F}}^{\mathrm{p}} \boldsymbol{F}^{\mathrm{p},-1}$ is the plastic distortion rate, and h is an internal stress-like variable related to the internal strain-like variable ξ as $h = -\partial\psi/\partial\xi$. Above, we do not include dissipation due to Darcian fluid flow, which occurs along the fluid pressure gradient, in $\mathcal{D}$. For reversible processes, $\mathcal{D} = 0$.

The last term above is the rate of work or power of faulting $\dot{\mathcal{W}}_f$, which can be approximated [34] as $\dot{\mathcal{W}}_f \approx T_f^{\mathrm{avg}} \times \dot{d}_f^{\mathrm{avg}} \times \Gamma_f^{\mathrm{slip}}$, where $T_f^{\mathrm{avg}} = (T_f^{\mathrm{aft}} + T_f^{\mathrm{bef}})/2$ is the average fault stress magnitude, $\dot{d}_f^{\mathrm{avg}} = (\dot{d}_f^{\mathrm{aft}} + \dot{d}_f^{\mathrm{bef}})/2$ is the average fault slip velocity magnitude, Γ_f^{slip} is the fault slip area, and the superscripts *bef* and *aft* indicate before and after the slip event. $\mathcal{W}_f$ can be decomposed into three parts: the heat released during slip, energy spent during creation of new material surfaces e.g. in the fault process zone, and the seismic radiation energy E_s. Ignoring the surface creation energy, which has been found to be 3-4 orders of magnitude smaller than the other terms, $E_s = \eta^{\mathrm{seis}} \mathcal{W}_f$, where $\eta^{\mathrm{seis}} = (T_f^{\mathrm{aft}} - T_f^{\mathrm{bef}})/(T_f^{\mathrm{aft}} + T_f^{\mathrm{bef}})$ is the seismic efficiency. Based on data from many earthquakes, it has been found that $\eta_{\mathrm{seis}} \leq 0.06$ [51]. The moment magnitude of the slip event can be obtained from the Hanks-Kanamori scale [52],

$$M_w = \frac{2}{3} \log_{10} \left(\frac{G \mathcal{W}_f}{T_f^{\mathrm{avg}}} \right) - 10.7 \tag{10}$$

It is also important to note that for a given drop in the free energy in Eq. (9), if $\mathcal{D}$ increases due to plastic dissipation, the energy available for faulting, $\mathcal{W}_f$, decreases. Our results in Section 4.3.2 provide further evidence for this hypothesis.

Poromechanics The kinematic or geometric nonlinearity can arise either in the form of large displacement/large rotation and large strain or large displacement/large rotation and small strain. Although both cases require the use of second Piola-Kirchhoff stress and Green-Lagrange strain tensors in the equilibrium and constitutive equations, modeling the former requires hyperelastic constitutive relations with large strain constitutive tensors. The latter behavior can be modeled by simply substituting $\boldsymbol{\sigma}'$ and $\boldsymbol{\varepsilon}$ with $\boldsymbol{S}'$ and $\boldsymbol{E}$, respectively. The small strain constitutive tensor does not change during this substitution [53].

In the finite strain theory, the requirement of frame indifference during material response means the material constitutive models are expressed in terms of the Lie derivative of the effective Kirchhoff stress, $\mathcal{L}_v \boldsymbol{\tau}'$. The relation between the total and effective stresses in the current configuration becomes

$$\mathcal{L}_v \boldsymbol{\tau}' = \mathcal{L}_v \boldsymbol{\tau} + b \dot{p}_e \boldsymbol{1}, \tag{11}$$

where $\mathcal{L}_v \boldsymbol{\tau} = \boldsymbol{F} \dot{\boldsymbol{S}} \boldsymbol{F}^{\mathrm{T}}$ is the Lie derivative of the total Kirchhoff stress, $\mathcal{L}_v \boldsymbol{\tau}' = \boldsymbol{F} \dot{\boldsymbol{S}}' \boldsymbol{F}^{\mathrm{T}}$ is the Lie derivative of the effective Kirchhoff stress, b is the Biot coefficient of the rock fully saturated with water or oil, and p_e is the saturation-weighted equivalent pore pressure defined as $p_e = s_w p_w + s_o p_o$ [54]. We treat the pore pressure derivative as the simple derivative, instead of the Lie derivative, given its scalar nature and independence from the coordinate system, so the formulation is objective.

The Biot coefficient is a tensor in anisotropic media [55,56]. We assume tensile stresses are positive. In the reference configuration Eq. (11) becomes

$$\dot{\boldsymbol{S}}' = \dot{\boldsymbol{S}} + b \dot{p}_e \boldsymbol{C}^{-1} \tag{12}$$

The effective stresses are responsible for the deformation of the material. In the current configuration, the rate form of this relation is

$$\mathcal{L}_v \boldsymbol{\tau}' = \mathbf{c} : \boldsymbol{d}, \tag{13}$$

where $J^{-1}\mathbf{c}$ is the rank-4 Eulerian elasticity tensor in the current configuration, $\boldsymbol{d} = \text{sym}[\boldsymbol{l}]$ is the rate of deformation tensor, and $\boldsymbol{l} = \nabla(\partial \boldsymbol{u}/\partial t) = \dot{\boldsymbol{F}}\boldsymbol{F}^{-1}$ is the gradient of Eulerian velocity vector $\partial \boldsymbol{u}/\partial t$. The stress-strain relation in the reference configuration becomes $\dot{\boldsymbol{S}}' = \mathbf{C} : \dot{\boldsymbol{E}}$ where $\dot{\boldsymbol{E}} = (1/2)\dot{\boldsymbol{C}} = \boldsymbol{F}^{\mathrm{T}} \cdot \boldsymbol{d} \cdot \boldsymbol{F}$ is the pull-back rule, and $\mathbf{C}$ is reference configuration's elastic constitutive tensor related to $\mathbf{c}$ as $\mathrm{c}_{ijkl} = 2F_{iA}F_{jB}F_{kC}F_{lD}\mathrm{C}_{ABCD}$ or $\boldsymbol{F}(\mathbf{C} : \dot{\boldsymbol{C}})\boldsymbol{F}^{\mathrm{T}} = \mathbf{c} : \boldsymbol{d}$. The incremental form of the pull-back rule provides a relation between the finite and infinitesimal strains as $\delta\boldsymbol{E} = \boldsymbol{F}^{\mathrm{T}}\delta\boldsymbol{\varepsilon}\boldsymbol{F}$. For a homogeneous isotropic linear elastic behavior, the elasticity tensor can be split as follows

$$\mathbf{c} = \left(k_{dr} - \frac{2G}{3}\right)\mathbf{1} \otimes \mathbf{1} + 2G\boldsymbol{I} = k_{dr}\mathbf{1} \otimes \mathbf{1} + 2G\boldsymbol{I}' \tag{14}$$

where $k_{dr} = (1/9)\mathbf{1} : \mathbf{c} : \mathbf{1}$ is the drained bulk modulus, $\boldsymbol{I}$ is the rank-4 identity tensor, $\boldsymbol{I}' = \boldsymbol{I} - \frac{1}{3}\mathbf{1} \otimes \mathbf{1}$ is the rank-4 deviatoric operator tensor, and G is the shear modulus. We assume constant elastic moduli and therefore no coupling between volumetric and deviatoric responses [40]. Also, we assume that $\mathbf{c}$ is independent of s_w and P_c. The Biot coefficient can be expressed as $b = 1 - (k_{dr}/k_s)$, where k_s is the solid grain modulus. Applying the trace operator to Eq. (11), we have

$$\mathcal{L}_v\boldsymbol{\tau}' : \mathbf{1} = \mathcal{L}_v\boldsymbol{\tau} : \mathbf{1} + 3b\dot{p}_e. \tag{15}$$

Using Eq. (13) and noting $\text{tr}[\boldsymbol{d}] = \boldsymbol{d} : \mathbf{1} = \dot{\varepsilon}_v$, we obtain

$$(\mathbf{c} : \boldsymbol{d}) : \mathbf{1} = 3k_{dr}\dot{\varepsilon}_v = \boldsymbol{F}\dot{\boldsymbol{S}}\boldsymbol{F}^{\mathrm{T}} : \mathbf{1} + 3b\dot{p}_e, \tag{16}$$

which resembles the effective stress relation in the infinitesimal formulation once we define, $\mathcal{L}_v\tau_v = \frac{1}{3}\boldsymbol{F}\dot{\boldsymbol{S}}\boldsymbol{F}^{\mathrm{T}} : \mathbf{1}$ and $\mathcal{L}_v\tau_v' = k_{dr}\dot{\varepsilon}_v$. The rate of deformation tensor can be split into volumetric and deviatoric parts: $\boldsymbol{d} = (1/3)\dot{\varepsilon}_v\mathbf{1} + \dot{\boldsymbol{e}}$, where $\boldsymbol{e}$ is the deviatoric strain tensor. The Green-Lagrange strain tensor can be split as $\dot{\boldsymbol{E}} = (1/3)\dot{\varepsilon}_v\boldsymbol{F}^{\mathrm{T}}\boldsymbol{F} + \boldsymbol{F}^{\mathrm{T}}\dot{\boldsymbol{e}}\boldsymbol{F}$.

In large displacement, large rotation, but small strain analysis (strain magnitude less than a couple percentages), material models developed for the infinitesimal strain analysis can be used directly, provided that $\boldsymbol{\sigma}'$ is substituted with the second PK stress tensor $\boldsymbol{S}'$, and $\boldsymbol{\varepsilon}$ is substituted with the Green-Lagrange strain tensor $\boldsymbol{E}$ [53]. This is possible because $\boldsymbol{S}'$ and $\boldsymbol{E}$, which are energy-conjugates, are invariant under rigid body motions (e.g., rotations of the grid cells of a reservoir/caprock layer deforming under fluid production). We apply the trace operator to Eq. (12) to write $\text{tr}[\dot{\boldsymbol{S}}'] = \text{tr}[\dot{\boldsymbol{S}}] + b\dot{p}_e\text{tr}[\boldsymbol{C}^{-1}]$. Defining $\dot{S}_v' = \text{tr}[\dot{\boldsymbol{S}}']$, $\dot{P}_e = \dot{p}_e\text{tr}[\boldsymbol{C}^{-1}]$, and splitting the strain tensor as $\dot{\boldsymbol{E}} = (1/3)\dot{E}_v\mathbf{1} + \dot{\boldsymbol{E}}_d$ and the stress tensor as $\dot{\boldsymbol{S}} = \dot{S}_v\mathbf{1} + \dot{\boldsymbol{s}}$, we have

$$\dot{S}_v' = K_{dr}\dot{E}_v = \dot{S}_v + b\dot{P}_e, \quad \dot{\boldsymbol{s}} = 2G\dot{\boldsymbol{E}}_d \tag{17}$$

where K_{dr} is defined from $\mathbf{C}$, and $\boldsymbol{s}$ and $\boldsymbol{E}_d$ are deviatoric stress and strain tensors. The first effective stress invariant can be defined as $I_1' = 3S_v'$ and the second invariant of the deviatoric stress can be defined as $J_2 = (1/2)\boldsymbol{s} : \boldsymbol{s}$. Using Eq. (12), we define the fault tractions as follows:

$$\sigma_n' = \left(\boldsymbol{F}\boldsymbol{S} + bp_f\boldsymbol{C}^{-1}\right) : \hat{\mathbf{n}}_f \otimes \hat{\mathbf{n}}_f, \quad \boldsymbol{\tau}_s = \boldsymbol{l}_f - \sigma_n'\hat{\mathbf{n}}_f \tag{18}$$

where p_f is the fault pressure modeled from the two pressures on the two sides of the fault [16,57].

Multiphase flow To express Eq. (5) in terms of the water phase pressure as the primary variable, we differentiate $M_w = \rho_w s_w \Phi$ and apply the chain rule:

$$\dot{M}_w = \rho_w(\Phi(c_w\dot{p}_w s_w + \dot{s}_w) + \dot{\Phi}s_w), \tag{19}$$

where we introduced the constitutive relation defining the water compressibility in the current configuration as $c_w = (1/\rho_w)d\rho_w/dp_w$, which allows the water density to be expressed in terms of the water pressure, e.g. $\rho_w = e^{c_w p_w}$. This defines the chemical potential of water as $\chi_w = \int(1/\rho_w)dp_w = \int_0^{p_w} e^{-c_w p_w}\, dp_w$. The $\dot{M}_o$ term in the oil mass conservation equation is similarly expressed in terms of the oil phase pressure p_o by using the oil compressibility c_o. We also define the saturation-weighted Lagrangian fluid density: $\rho_f^0 = (\rho_w^0 s_w + \rho_o^0 s_o)$.

We assume pressure-dependent fluid viscosities μ_w and μ_o. Additional constitutive relations are required for k_{rw}, k_{ro} and P_c. We use Corey-type relation for the relative permeabilities and van Genuchten-type relation for the capillary pressure, both of which are expressed as analytical functions of s_w (the wetting phase saturation). We discuss the capillary relation in more detail in the flow rules section below.

The constitutive equation of poroelasticity states that the fluid mass increment has two contributions, the volumetric expansion of the skeleton and the increment in fluid pressure [58],

$$\begin{aligned}
\frac{\dot{M}_w}{\rho_w^0} &= \left(b_w\dot{\varepsilon}_v + N_{ww}\dot{p}_w + N_{wo}\dot{p}_o\right), \\
\frac{\dot{M}_o}{\rho_o^0} &= \left(b_o\dot{\varepsilon}_v + N_{wo}\dot{p}_w + N_{oo}\dot{p}_o\right)
\end{aligned} \tag{20}$$

where $\boldsymbol{N} = [N_{ww}, N_{wo}; N_{wo}, N_{oo}] = \boldsymbol{M}_b^{-1}$ is the 2×2 inverse Biot modulus matrix in the current configuration. Denoting the Biot modulus matrix in the reference configuration as $\boldsymbol{M}_b^0$, we have $\boldsymbol{M}_b = J^{-1}\boldsymbol{M}_b^0$. $b_w = bs_w$ and $b_o = bs_o$ are the fluid-specific Biot coefficients. Components of the $\boldsymbol{N}$ matrix can be expressed in terms of rock and fluid properties [59,16]. For example, for water-saturated conditions ($s_w = 1$) or single-phase flow, $M_b = \left(\phi c_w + (b - \phi^0)/k_s\right)^{-1}$.

Fault slip The normal force on the fault is always compressive except when the two sides loose contact at which time the normal force becomes zero. Along with the no-interpenetration condition, this implies the following Kuhn-Tucker conditions: $\sigma_n' \le 0,\ d_n \ge 0,\ \sigma_n' d_n = 0$. We define the stick-slip behavior of the fault in terms of σ_n', $|\boldsymbol{\tau}_s|$, and the fault friction stress $\tau_c - \mu_f \sigma_n'$, where μ_f is the coefficient of fault friction and τ_c is the fault cohesion. Here, $|\cdot|$ is the magnitude operator or Euclidean norm of a vector. We use the Mohr-Coulomb (M-C) stick-slip condition to determine when a point on the fault slips. The condition is,

$$f_s = |\boldsymbol{\tau}_s| - \tau_c + \mu_f \sigma_n' \le 0, \tag{21}$$

i.e., there is no slip until the shear traction magnitude is less than the friction stress, otherwise there is slip and relaxation of fault stresses. f_s is also known as the Coulomb Failure Function (CFF) in the induced seismicity literature [16]. Tracking the change in CFF, as injection or production continues in the reservoir, is a standard method of assessing and mitigating the induced seismicity hazard [11,17]. Initial conditions of a simulation are chosen such that all points on the surface of the fault satisfy the above condition. As the reservoir pressure and stress change with the well operation, $|\boldsymbol{\tau}_s|$ and σ_n' change on the fault. If the changes are destabilizing, e.g. increasing shear and/or decreasing compression, the condition is violated and the fault slips. We define the hypocenter as the fault node where the M-C condition is violated earliest in time. We use the slip-weakening relation to capture the rapid drop in μ_f immediately after the onset of slip, which is commonly observed in earthquakes [34]. Slip weakening allows the fault friction coefficient to decrease from its static value μ_s to a dynamic value μ_d over the critical slip distance d_c.

$$\mu_f = \begin{cases} \mu_s - (\mu_s - \mu_d)\frac{|\boldsymbol{d}_s|}{d_c}, & |\boldsymbol{d}_s| \le d_c, \\ \mu_d, & |\boldsymbol{d}_s| > d_c. \end{cases} \tag{22}$$

Poroplasticity Assuming an isotropic response and using $\boldsymbol{\tau}' = \boldsymbol{F}^{\mathrm{e}} \boldsymbol{S}' \boldsymbol{F}^{\mathrm{e,T}}$, the hyperelastic constitutive relation can be written in terms of $\boldsymbol{b}^{\mathrm{e}}$ and either $\boldsymbol{\tau}'$ or $\boldsymbol{S}'$ as

$$\boldsymbol{\tau}' = 2\frac{\partial \psi}{\partial \boldsymbol{b}^{\mathrm{e}}}\boldsymbol{b}^{\mathrm{e}}, \quad \boldsymbol{S}' = 2\boldsymbol{F}^{\mathrm{e},-1}\frac{\partial \psi}{\partial \boldsymbol{b}^{\mathrm{e}}}\boldsymbol{F}^{\mathrm{e}} \tag{23}$$

To completely specify a poro-elastoplastic problem, three components are needed–a yield condition, flow rules based on a plastic potential, and a hardening or softening rule. The yield condition specifies the state of stress at which plastic flow initiates, and the potential function is used to determine the magnitude and direction of plastic strain and other internal state variables such as the plastic porosity. The yield condition is generally written in the following form

$$f_p\left(\boldsymbol{S}, p_e, P_c, h\right) = f_p\left(\boldsymbol{\tau}', P_c, h\right) \le 0. \tag{24}$$

The potential function for drained plastic flow is given in the form

$$g_p\left(\boldsymbol{S}, p_e, P_c, h\right) = g_p\left(\boldsymbol{\tau}', P_c, h\right) \le 0. \tag{25}$$

A non-associative model ($f_p \ne g_p$) ensures that the direction of plastic strain rate vector is not perpendicular to the yield surface. Non-associated models can address the issue of unreasonable amounts of dilatation that are sometimes predicted by the associated model ($f_p = g_p$), which is based on the assumption of maximum plastic dissipation. In multiphase geomechanics, non-associativity often arises from the commonly-used models for the capillary pressure-saturation relation.

2.4.1. Flow rules

To determine the amount and direction of plastic deformation (plastic flow rule) in large displacement/rotation–large strain, first we look at the material time derivative of $\boldsymbol{b}^{\mathrm{e}}$:

$$\dot{\boldsymbol{b}}^{\mathrm{e}} = \boldsymbol{l}\boldsymbol{b}^{\mathrm{e}} + \boldsymbol{b}^{\mathrm{e}}\boldsymbol{l} + \mathcal{L}_v \boldsymbol{b}^{\mathrm{e}} \tag{26}$$

where $\boldsymbol{l} = \boldsymbol{l}^{\mathrm{e}} + \boldsymbol{l}^{\mathrm{p}}$ with $\boldsymbol{l}^{\mathrm{e}} = \dot{\boldsymbol{F}}^{\mathrm{e}}\boldsymbol{F}^{\mathrm{e},-1}$ and $\boldsymbol{l}^{\mathrm{p}} = \boldsymbol{F}^{\mathrm{e}}\boldsymbol{L}^{\mathrm{p}}\boldsymbol{F}^{\mathrm{e},-1}$. The Lie derivative of the strain is

$$\mathcal{L}_v \boldsymbol{b}^{\mathrm{e}} = \boldsymbol{F}\frac{d\boldsymbol{C}^{\mathrm{p},-1}}{dt}\boldsymbol{F}^{\mathrm{T}} = \boldsymbol{F}\frac{d}{dt}\left[\boldsymbol{F}^{-1}\boldsymbol{b}^{\mathrm{e}}\boldsymbol{F}^{-T}\right]\boldsymbol{F}^{\mathrm{T}} = -2\boldsymbol{F}^{\mathrm{e}}\mathrm{sym}[\boldsymbol{L}^{\mathrm{p}}]\boldsymbol{F}^{\mathrm{e,T}}. \tag{27}$$

Maximization of the dissipation $\mathcal{D}$ resulting from Eq. (9) provides us with the flow rules for the plastic volumetric strain and plastic mass content [38]. The former is

$$-\frac{1}{2}(\mathcal{L}_v \boldsymbol{b}^{\mathrm{e}})\boldsymbol{b}^{\mathrm{e},-1} = \dot{\lambda}\frac{\partial g_p}{\partial \boldsymbol{\tau}'} \tag{28}$$

where $\dot{\lambda}$ is the plastic multiplier and $\partial g_p/\partial \boldsymbol{\tau}'$ is the gradient tensor of the plastic potential function with respect to the effective Kirchhoff stress. The incremental plastic volumetric strain can be computed as

$$\dot{\varepsilon}_v^{\mathrm{p}} = \frac{\dot{J}^{\mathrm{p}}}{J^{\mathrm{p}}} = \dot{\boldsymbol{F}}^{\mathrm{p}} : \boldsymbol{F}^{\mathrm{p,-T}} = \dot{\boldsymbol{F}}^{\mathrm{p}}\boldsymbol{F}^{\mathrm{p},-1} : \mathbf{1} = \mathrm{tr}[\boldsymbol{L}^{\mathrm{p}}] \tag{29}$$

The elastoplastic tangent modulus $\mathbf{c}^{\mathrm{ep}}$ can be obtained from $\dot{\boldsymbol{\tau}}' = \mathbf{c} : (\boldsymbol{d} - \dot{\lambda}\partial g_p/\partial \boldsymbol{\tau}') = \mathbf{c}^{\mathrm{ep}} : \boldsymbol{d}$. Associative plasticity models guarantee that the elastoplastic tangent tensors are symmetric.

Flow rule for plastic fluid mass increments can also be obtained from the dissipation maximization principle. For the water phase, we obtain

$$\dot{M}_w^{\mathrm{p}} = \rho_w^0 \dot{\lambda}\frac{\partial g_p}{\partial p_w} = -bs_w\rho_w^0\dot{\lambda}\left(\frac{\partial g_p}{\partial \boldsymbol{\tau}'} : \mathbf{1}\right) \tag{30}$$

where it is the assumed that the fluid compressibility over a time increment is small. Substituting sequentially from Eq. (28), Eq. (27), and Eq. (29), we obtain

$$\dot{M}_w^{\mathrm{p}} = bs_w\rho_w^0\frac{1}{2}(\mathcal{L}_v \boldsymbol{b}^{\mathrm{e}})\boldsymbol{b}^{\mathrm{e},-1} : \mathbf{1} = bs_w\rho_w^0\dot{\varepsilon}_v^{\mathrm{p}}, \qquad \dot{\varepsilon}_v^{\mathrm{p}} = \dot{\lambda}\cdot\mathrm{tr}\left[\frac{\partial g_p}{\partial \boldsymbol{\tau}'}\right] \tag{31}$$

Flow rule for $\dot{s}_w$ can be written in terms of the plastic multiplier and the gradient of the yield function with respect to P_c, $\dot{s}_w = -\dot{\lambda}(\partial f_p/\partial P_c)$, which can be written as $\dot{s}_w = (\partial s_w/\partial P_c)\dot{P}_c$. Another candidate formulation is

$$\dot{s}_w = \frac{\partial s_w}{\partial J}\dot{J} + \frac{\partial s_w}{\partial P_c}\left(\dot{P}_c + \frac{\dot{J}}{J}P_c\right), \tag{32}$$

which makes the capillary pressure a function of deformation: ε_v and ϕ. As mentioned above, we use a van Genuchten-type relation that qualifies as a non-associative flow rule for $\dot{s}_w$. However, following [58], we assume that the effect of deformation on the capillary relation is negligible by neglecting the $\dot{J}$ terms. This makes our relative permeability relations, k_{rw} and k_{ro} vs. s_w, also independent of deformation.

The evolution of plastic multiplier is subject to the Kuhn-Tucker loading/unloading conditions:

$$\dot{\lambda} \geq 0, \quad f_p \leq 0, \quad \dot{\lambda} f_p = 0, \tag{33}$$

and the consistency condition,

$$\dot{f}_p(\boldsymbol{S}, p_e, P_c, h) = 0, \tag{34}$$

based on which we obtain

$$\dot{\lambda} = \frac{(\partial f_p/\partial \boldsymbol{\tau}') : \mathbf{c} : \boldsymbol{l}}{(\partial f_p/\partial \boldsymbol{\tau}') : \mathbf{c} : (\partial g_p/\partial \boldsymbol{\tau}')}. \tag{35}$$

For large displacement/rotation–small strain, we use the plastic flow rule written in terms of $\boldsymbol{S}'$:

$$\dot{\boldsymbol{\varepsilon}}^{\mathrm{p}} = \dot{\lambda}\frac{\partial g_p}{\partial \boldsymbol{S}'}, \tag{36}$$

and the plastic volumetric strain is calculated from its trace. The elastoplastic tangent modulus $\mathbf{C}^{\mathrm{ep}}$ is defined as $\dot{\boldsymbol{S}}' = \mathbf{C} : (\dot{\boldsymbol{E}} - \dot{\boldsymbol{\varepsilon}}^{\mathrm{p}}) = \mathbf{C}^{\mathrm{ep}} : \dot{\boldsymbol{E}}$.

Finally, the hardening rule can be written as $\dot{h} = \dot{\lambda}\partial g_p/\partial \xi$. The hardening rule describes how the yield condition and flow rule are modified during plastic flow. For no hardening and perfectly plastic material, the yield condition and flow rule remain constant during plastic flow.

2.4.2. Drucker-Prager model

We consider the Drucker-Prager (D-P) elastoplastic model [42] to describe the behavior of reservoir and caprock under flow-induced loading. The D-P yield surface, which is a smooth approximation of the M-C yield surface for continuum modeling of yielding in 3D, has been used in the literature to model plastic deformation of soils and rocks. For large displacement/rotation–small strain, the model can be written in terms of $\boldsymbol{S}'$ and $\boldsymbol{E}$ [53]. We define a yield condition for perfect plasticity and with capillarity as follows

$$f_p\,(\boldsymbol{S}, P_c, p_e) = \alpha_f(S_v + \beta P_e) + \sqrt{J_2} - \gamma - \zeta P_c \leq 0, \tag{37}$$

and the plastic potential is given by

$$g_p(\boldsymbol{S}, p_e) = \alpha_g(S_v + \beta P_e) + \sqrt{J_2}, \tag{38}$$

where α_f, α_g, β, γ, and ζ are model constants. Here, β accounts for the plastic volumetric strain of the solid matrix ($\phi^0 \leq \beta \leq 1$) and can be assumed equal to the Biot coefficient [58]. A $\zeta > 0$ value can extend the yield surface to the tensile region and allow tensile failure. To calculate increments in plastic strain and plastic fluid mass, we need gradients of functions f_p and g_p. Note that

$$df_p = \frac{\partial f_p}{\partial \boldsymbol{S}} : \boldsymbol{dS} + \frac{\partial f_p}{\partial p_e} dp_e. \tag{39}$$

Substituting Eq. (38) in Eq. (36), we obtain the rates of increment in plastic strain and fluid mass of slightly compressible fluids,

$$\dot{\boldsymbol{\varepsilon}}^{\mathrm{p}} = \dot{\lambda}\left(\frac{\alpha_g}{3}\mathbf{1} + \frac{1}{2\sqrt{J_2}}\boldsymbol{s}\right), \quad \dot{M}^{\mathrm{p}} = \dot{\lambda}\alpha_g\beta\rho_f^0. \tag{40}$$

2.5. Effect of finite strain plasticity on the flow problem

It is important to understand the effect of plastic strain on the solution of the flow problem, especially within an iterative solution scheme where the flow and mechanics problems are solved sequentially. Therefore, we can re-write the fluid mass increment Eqs. (20) explicitly in terms of the plastic strain. For example, for water,

$$\dot{M}_w = \rho_w^0\left[\sum_{N=o,w}\left(\frac{b_w b_N}{k_{dr}} + N_{wN}\right)\dot{p_N} + \frac{b_w}{k_{dr}}\mathcal{L}_v\tau_v + b_w\dot{\varepsilon}_v^{\mathrm{p}}\right], \tag{41}$$

which can be combined with Eq. (19) to obtain the porosity evolution equation,

$$\frac{1}{J}\dot{\Phi} = \frac{b}{k_{dr}}\mathcal{L}_v\tau_v + \sum_{N=o,w}\left(\frac{b^2 s_N}{k_{dr}} + \frac{(b-\phi^0)s_N}{k_s}\right)\dot{p_N} + b\dot{\varepsilon}_v^{\mathrm{p}} \tag{42}$$

Substituting Eq. (41) in Eq. (5) gives us the water phase equation:

$$\sum_{N=o,w}\left(\frac{b_w b_N}{k_{dr}} + N_{wN}\right)\dot{p_N} + \frac{b_w}{k_{dr}}\mathcal{L}_v\tau_v + b_w\dot{\varepsilon}_v^{\mathrm{p}} + \frac{1}{\rho_w}\nabla\cdot\boldsymbol{w}_w + \frac{q_w}{\rho_w} = 0, \tag{43}$$

which is analogous to the pressure equation under infinitesimal deformation (Eq. (30) in [16]). The oil phase equation is obtained similarly. For large displacement/rotation–small strain, $\mathcal{L}_v\tau_v$ is substituted with $\dot{S}_v$, and k_{dr} is substituted with K_{dr}. This suggests that the fixed stress iterative solution scheme for infinitesimal deformation can be extended to finite strain plasticity by fixing $\left(\dot{S}_v, \dot{\varepsilon}_v^{\mathrm{p}}\right)$ during the solution of the flow problem.

3. Numerical model

Below we present the numerical solution model for the problem described in the previous section. First, we present the weak forms of the mechanics and flow sub-problems while accounting for finite strain plasticity and fault slip. Next, we linearize the equations that need to be solved to simulate the dynamics of fluid flow, finite strain geomechanics, and fault slip processes in the domain. Then we describe our sequential iterative solution strategy which entails solving the flow problem in a Newton loop while freezing the variations in the total volumetric stress and the volumetric plastic strain, followed by solving the mechanics problem in another Newton loop while freezing the fluid pressure and saturations.

3.1. Weak forms

The weak form of Eq. (6) in Lagrangian coordinates is obtained by following the standard variational recipe: take the dot product of the strong form with a test function $\boldsymbol{\eta}$ belonging to a suitable space of vector functions (zero for the material points on the prescribed displacement boundary of the body), integrate over the reference volume, use integration by parts, and apply the divergence theorem. The result is [60],

$$\int_{V^0} \boldsymbol{P} : \nabla_X\boldsymbol{\eta}\, dV^0 = \int_{\Gamma_\sigma^0} \overline{\boldsymbol{T}}\cdot\boldsymbol{\eta}\, d\Gamma_\sigma^0 + \int_{V^0}\rho_b^0\boldsymbol{g}\cdot\boldsymbol{\eta}\, dV^0 \tag{44}$$

where Γ^0_σ is the Neumann (traction) boundary in the reference configuration, $\overline{\boldsymbol{T}} = \boldsymbol{P}\hat{\boldsymbol{n}}$ is the prescribed traction vector on that boundary, and $\hat{\boldsymbol{n}}$ is the outward unit normal to the boundary. Prescribed displacement and prescribed traction boundaries do not overlap and their union equals the complete boundary. For time-dependent tectonic boundary conditions, Eq. (44) can be written in the rate form with $\dot{\boldsymbol{P}} = (\dot{\boldsymbol{F}}\boldsymbol{S} + \dot{\boldsymbol{S}}\boldsymbol{F})$ in place of $\boldsymbol{P}$. Since we consider constant boundary conditions and use a sequential iterative solution scheme where pressure is frozen during mechanics solve (details below), the weak form in Eq. (44) is sufficient. Since $\boldsymbol{S}$ is symmetric, we have $\boldsymbol{P} : \nabla_X \boldsymbol{\eta} = \boldsymbol{S} : \mathrm{sym}[\nabla_X \boldsymbol{\eta} \cdot \boldsymbol{F}^{\mathrm{T}}]$. Defining the virtual strain as $\delta\boldsymbol{E} = \mathrm{sym}[\nabla_X \boldsymbol{\eta} \cdot \boldsymbol{F}^{\mathrm{T}}]$, where the variation δ is taken about the current configuration, we can write the weak form as

$$\int_{V^0} (\boldsymbol{S}' - bp_e \boldsymbol{C}^{-1}) : \delta\boldsymbol{E}\, dV^0 = \int_{\Gamma^0_\sigma} \overline{\boldsymbol{T}} \cdot \boldsymbol{\eta}\, d\Gamma^0_\sigma + \int_{V^0} \rho^0_b \boldsymbol{g} \cdot \boldsymbol{\eta}\, dV^0. \tag{45}$$

The left hand side above is the internal virtual work and the right hand side is the external virtual work. The traction continuity equation across the fault, $\boldsymbol{T}^+_f = \boldsymbol{T}^-_f$, contributes two surface integral terms to the internal virtual work, corresponding to tractions on Γ_+ and Γ_- sides of the fault [16]:

$$\begin{aligned} &\int_{V^0 \setminus \Gamma_f} (\boldsymbol{S}' - bp_e \boldsymbol{C}^{-1}) : \delta\boldsymbol{E}\, dV^0 + \int_{\Gamma^0_+} \boldsymbol{\eta}^{\mathrm{T}} (\boldsymbol{l}_f - bp_f \boldsymbol{F}^{-\mathrm{T}} \hat{\boldsymbol{n}}_f)\, d\Gamma^0 \\ &- \int_{\Gamma^0_-} \boldsymbol{\eta}^{\mathrm{T}} (\boldsymbol{l}_f - bp_f \boldsymbol{F}^{-\mathrm{T}} \hat{\boldsymbol{n}}_f)\, d\Gamma^0 - \int_{\Gamma^0_\sigma} \overline{\boldsymbol{T}} \cdot \boldsymbol{\eta}\, d\Gamma^0_\sigma - \int_{V^0} \rho^0_b \boldsymbol{g} \cdot \boldsymbol{\eta}\, dV^0 = R_u = 0, \end{aligned} \tag{46}$$

where p_f is the fault pressure related to the pressures on the two sides of the fault [16], e.g. footwall and hanging wall block pressures in case of a dip-slip fault, and R_u is the mechanics residual. We use the Lagrange multiplier method to impose contact forces at the fault that are required to honor the stick-slip condition. As a result, the Lagrange multipliers acquire the physical meaning of the fault tractions $\boldsymbol{l}_f$ defined in Eq. (18). Also, they become unknowns of the problem, similar to the displacements. We use piecewise linear displacement test functions with nodal displacement degrees of freedom (d.o.f.) $\boldsymbol{U}$ and piecewise linear fault traction test functions with traction d.o.f. $\boldsymbol{L}_f$ on the Lagrange (fault) nodes to discretize the mechanics weak form. In this study, we use a trilinear hexahedral finite element mesh with bilinear quadrilaterals on the 2D fault surface. The residual is evaluated at each integration point in each element. The weak form of the fault slip equation, Eq. (8), is

$$\int_{\Gamma_+} \boldsymbol{\eta} \cdot \boldsymbol{u}^+ d\Gamma - \int_{\Gamma_-} \boldsymbol{\eta} \cdot \boldsymbol{u}^- d\Gamma - \int_{\Gamma_f} \boldsymbol{\eta} \cdot \boldsymbol{d}_f d\Gamma = R_l = 0, \tag{47}$$

where R_l is the fault residual evaluated at the Lagrange (fault) nodes. The fault slip is discretized using the same test functions as the fault traction. We denote the slip d.o.f. by $\boldsymbol{D}_f$.

The weak form of the multiphase flow problem is obtained by applying the same variational recipe to water and oil mass conservation equations. For water, Eq. (5) gives

$$\int_{V^0} \dot{M}_w \eta_p\, dV^0 - \int_{\Gamma^0_w} \overline{W} \eta_p\, d\Gamma^0_w - \int_{V^0} J\boldsymbol{w}_w \cdot \nabla\eta_p\, dV^0 + \int_{V^0} J q_w \eta_p\, dV^0 = R_w = 0, \tag{48}$$

where η_p is the pressure or saturation test function (zero on the fixed pressure boundary), $\overline{W} = J\boldsymbol{F}^{-1}\boldsymbol{w}_w \cdot \hat{\boldsymbol{n}}$ is the prescribed normal mass flux on the flux boundary Γ^0_w in the reference configuration, and R_w denotes the residual for the water equation. The internal flux term is expressed in terms of the product of the fluid phase mobility $\boldsymbol{k}k_{rw}/\mu_w$ and the phase pressure gradient p_w using Darcy's relation. Similarly, we have the weak form of the oil phase, which we write in the residual form as $R_o = 0$. We use the finite volume method to discretize the weak forms of the flow problem using piecewise constant η_p ($\nabla\eta_p = \boldsymbol{0}$) and element-centered d.o.f. for the oil phase pressure P_o and the water phase saturation S_w. P_w is obtained from the capillary pressure relation, and S_o is obtained from the saturation constraint. We use backward Euler time integration method to discretize the time derivative of fluid mass. We evaluate R_o and R_w for each mesh element.

3.2. Mechanics model

We use the Total Lagrangian method [53] to linearize the mechanical equilibrium equations. Denoting the body configuration at t^{n+1} as $\boldsymbol{x}^{n+1} = \boldsymbol{x}^n + \boldsymbol{du}$, the incremental decomposition relations are,

$$\boldsymbol{S}'^{,n+1} = \boldsymbol{S}'^{,n} + \boldsymbol{dS}', \quad \boldsymbol{E}^{n+1} = \boldsymbol{E}^n + \boldsymbol{dE}, \quad \boldsymbol{u}^{n+1} = \boldsymbol{u}^n + \boldsymbol{du} \tag{49}$$

The deformation gradient at t^{n+1} can be written as

$$\begin{aligned}\boldsymbol{F}^{n+1} &= \frac{\partial \boldsymbol{x}^{n+1}}{\partial \boldsymbol{X}} = \frac{\partial \boldsymbol{x}^{n}}{\partial \boldsymbol{X}} + \frac{\partial \boldsymbol{du}}{\partial \boldsymbol{x}^{n}}\frac{\partial \boldsymbol{x}^{n}}{\partial \boldsymbol{X}} \\ &= [\boldsymbol{1} + \nabla_{\boldsymbol{x}^n}\boldsymbol{du}]\,\boldsymbol{F}^{n} = \boldsymbol{f}^{n+1}\boldsymbol{F}^{n}\end{aligned} \tag{50}$$

where $\boldsymbol{f}^{n+1} = \boldsymbol{1} + \left(\partial \boldsymbol{du}/\partial \boldsymbol{x}^{n}\right)$ is known as the relative deformation gradient [60,54]. From the definition of the incremental strain [53],

$$\begin{aligned}\boldsymbol{dE} &= \mathrm{sym}\left[\nabla_X \boldsymbol{du} + (\nabla_X \boldsymbol{u}^n)(\boldsymbol{du}\nabla_X)\right] + \frac{1}{2}(\nabla_X \boldsymbol{du})(\boldsymbol{du}\nabla_X) \\ &= \boldsymbol{dE}_{\mathrm{L}} + \boldsymbol{dE}_{\mathrm{NL}}\end{aligned} \tag{51}$$

where $\boldsymbol{dE}_{\mathrm{L}}$ is the linear part of the incremental strain (linear in $\boldsymbol{du}$) and $\boldsymbol{dE}_{\mathrm{NL}}$ is the nonlinear part. Noting that $\boldsymbol{\delta E}^n = \boldsymbol{0}$, the integrand in the stiffness term on the left hand side of Eq. (46) can be linearized as follows

$$\begin{aligned}\boldsymbol{S}'^{,n+1} : \boldsymbol{\delta E}^{n+1} &= \boldsymbol{dS}' : \boldsymbol{\delta dE} + \boldsymbol{S}'^{,n} : \boldsymbol{\delta dE}_{\mathrm{NL}} + \boldsymbol{S}'^{,n} : \boldsymbol{\delta dE}_{\mathrm{L}} \\ &\approx \left(\frac{\partial \boldsymbol{S}'^{,n}}{\partial \boldsymbol{E}^{n}} : \boldsymbol{dE}_{\mathrm{L}}\right) : \boldsymbol{\delta dE}_{\mathrm{L}} + \boldsymbol{S}'^{,n} : \boldsymbol{\delta dE}_{\mathrm{NL}} + \boldsymbol{S}'^{,n} : \boldsymbol{\delta dE}_{L}\end{aligned} \tag{52}$$

where second and higher order $\boldsymbol{du}$ terms have been dropped from the Taylor expansion of the first term, the second term is already linear because $\boldsymbol{\delta dE}_{\mathrm{NL}}$ is linear in $\boldsymbol{du}$, and the third term is independent of $\boldsymbol{du}$. Linearization of the mechanics weak form gave rise to the algorithmic tangent operator, $\partial \boldsymbol{S}'^{,n}/\partial \boldsymbol{E}^n$, which we denote by $\mathbf{D}^n$. It replaces the constitutive elasto-plastic tensor ($\mathbf{c}^{\mathrm{ep}}$ in large deformation–large strain or $\mathbf{C}^{\mathrm{ep}}$ in large deformation–small strain) and ensures that Newton's method for the mechanics solver can converge quadratically when close to the solution [60,61]. In Appendix, we provide the expression for $\mathbf{D}$ for our Drucker-Prager elastoplastic material. Discretization results in $\boldsymbol{dE}_{\mathrm{L}} = \boldsymbol{B}^n_{\mathrm{L}}\boldsymbol{dU}$ and $\boldsymbol{dE}_{\mathrm{NL}} = \boldsymbol{B}_{\mathrm{NL}}\boldsymbol{dU}$, where $\boldsymbol{B}_{\mathrm{L}}$ and $\boldsymbol{B}_{\mathrm{NL}}$ are linear and nonlinear strain-displacement matrices. The linear strain-displacement matrix contains products of the shape function derivative and $\boldsymbol{u}^n$, and hence has a superscript n. Strain variations are discretized similarly.

The discrete linear system of the mechanics problem now has two types of unknowns: the displacement d.o.f. $\boldsymbol{U}$ at the displacement nodes and the fault traction d.o.f. $\boldsymbol{L}_f$ at the fault nodes. We solve the system using Newton's method. Eqs. (49) and (52) are written with (k) and $(k+1)$ substituting for n and $n+1$, i.e. $[\boldsymbol{U}, \boldsymbol{L}_f]^{(k+1)} = [\boldsymbol{U}, \boldsymbol{L}_f]^{(k)} + [\boldsymbol{dU}, \boldsymbol{dL}_f]$, where (k) is the Newton iteration counter at t^{n+1}, and the correction vector is the solution to the system of linear equations:

$$\begin{bmatrix}\boldsymbol{K} & \boldsymbol{C}_l^{\mathrm{T}} \\ \boldsymbol{C}_l & \boldsymbol{0}\end{bmatrix}^{(k)}\begin{bmatrix}\boldsymbol{dU} \\ \boldsymbol{dL}_f\end{bmatrix} = -\begin{bmatrix}\boldsymbol{R}_u \\ \boldsymbol{R}_l\end{bmatrix}^{(k)}, \tag{53}$$

where the stiffness matrix $\boldsymbol{K}$ and the direction cosine matrix $\boldsymbol{C}_l$, which converts from the global coordinate system to the fault coordinate system, are obtained via element-by-element assembly of the nodal contributions from the displacement nodes and the fault nodes. $\boldsymbol{R}_u = [R_u]$ and $\boldsymbol{R}_l = [R_l]$ are vectors of residuals. The element stiffness matrix for element i is obtained as follows:

$$\boldsymbol{K}_i^{(k)} = \frac{\partial \boldsymbol{R}_{u,i}^{(k)}}{\partial \boldsymbol{U}_i^{(k)}} = \int_{V^0}\left(\boldsymbol{B}_{\mathrm{L},i}^{(k),\mathrm{T}}\mathbf{D}_i^{(k)}\boldsymbol{B}_{\mathrm{L},i}^{(k)} + \boldsymbol{B}_{\mathrm{NL},i}^{(k),\mathrm{T}}\boldsymbol{S}_i'^{,(k)}\boldsymbol{B}_{\mathrm{NL},i}^{(k)}\right)dV^0 \tag{54}$$

which has a linear part with the elastoplastic tensor and a nonlinear part with the stress tensor $\boldsymbol{S}_i'^{,(k)}$. The third term in Eq. (52) becomes $\boldsymbol{S}'^{,(k)} : \boldsymbol{\delta E}^{(k)}$, which is known and does not contribute to the stiffness matrix but appears as $\boldsymbol{B}_{\mathrm{L},i}^{(k)}\boldsymbol{S}_i'^{,(k)}$ in $R_{u,i}^{(k)}$. The pore pressure term in Eq. (46) does not contribute to the stiffness matrix because we freeze the pressure during the mechanics solve as per the sequential iterative solution scheme mentioned earlier. In Newton's method, an error in the residual implies convergence to an incorrect solution and an error in the system Jacobian implies a slower rate of convergence. Since $\boldsymbol{S}'$ is inside R_u, the stress path must be evaluated accurately during the simulation otherwise the simulation will diverge away from the true solution. Eq. (53) is a saddle point problem resulting from the use of the Lagrange multiplier method to solve the fault contact problem. To solve this system, we use the field split preconditioner option in PETSc [62,63], which allows us to use two different preconditioners for the elasticity and the fault sub-blocks. We use an algebraic multigrid preconditioner for the former and an approximation of the Schur complement of $\boldsymbol{K}$ for the latter [63]. The Schur complement is $-\boldsymbol{C}_l\boldsymbol{K}^{-1}\boldsymbol{C}_l^{\mathrm{T}}$ and it is approximated with a sum of two terms corresponding to displacement nodes on the positive and negative sides of the fault [63]. Since only fault side nodes are involved, the Schur approximation is fast to compute.

3.2.1. Poroplastic model

Large displacement/rotation–large strain First, we describe the model for large displacement, large rotations, and large strain, which may be more applicable to reservoirs with small aspect ratios (similar dimensions in different principal stress directions) and brittle rocks. The left Cauchy-Green tensor at t^n is calculated as $\boldsymbol{b}^{\mathrm{e},n} = \boldsymbol{F}^{\mathrm{e},n}\boldsymbol{F}^{\mathrm{e},\mathrm{T},n}$. Then Eq. (23) is used to

evaluate $\boldsymbol{\tau}'^{,n}$. An elastic predictor–plastic corrector scheme, which is a type of return-mapping algorithm [38,54], is used to solve the elastoplastic problem and determine $\boldsymbol{b}^{\mathrm{e},n+1}$, $\boldsymbol{\tau}'^{,n+1}$, and $\boldsymbol{S}'^{,n+1}$. The predictor step gives the trial state as

$$\boldsymbol{b}^{\mathrm{e},tr} = \boldsymbol{f}^{n+1}\boldsymbol{b}^{\mathrm{e},n}\boldsymbol{f}^{n+1,\mathrm{T}},\ \boldsymbol{\tau}'^{,tr} = 2\boldsymbol{b}^{\mathrm{e},tr}(\partial\psi/\partial\boldsymbol{b}^{\mathrm{e},tr}),\ M^{\mathrm{p},tr} = M^{\mathrm{p},n}. \tag{55}$$

where P_c is assumed constant because we freeze pore pressures during the mechanics solve. If the yield condition is satisfied with the trial state, i.e. $f_p^{tr} < 0$, we have zero plastic flow during this time step and $\boldsymbol{b}^{\mathrm{e},n+1} = \boldsymbol{b}^{\mathrm{e},tr}$, $M^{\mathrm{p},n+1} = M^{\mathrm{p},tr}$. If the condition is not satisfied, we have plastic flow and the corrector step calculates the correction to be added to $\boldsymbol{b}^{\mathrm{e},tr}$. This correction, as per Eq. (26), is the Lie derivative of $\boldsymbol{b}^{\mathrm{e},n+1}$:

$$\mathcal{L}_v\boldsymbol{b}^{\mathrm{e},n+1} = -2\dot{\lambda}\sum_{i=1}^{3}\frac{\partial g}{\partial\tau_i'}\theta_i^{\mathrm{e},n+1}\boldsymbol{m}^i, \quad \text{where } \boldsymbol{m}^i = \boldsymbol{n}^i\otimes\boldsymbol{n}^i, \tag{56}$$

$\theta_i^{\mathrm{e},n+1}$ are the three principal values (eigenvalues) of $\boldsymbol{b}^{\mathrm{e},n+1}$ obtained from the spectral decomposition: $\boldsymbol{b}^{\mathrm{e},n+1} = \sum_i \theta_i^{\mathrm{e},n+1}\boldsymbol{m}^i$, τ_i' are the principal values of $\boldsymbol{\tau}'^{,n+1}$, and $\boldsymbol{n}^i$ are the principal directions or eigenvectors (same for both the stress and strain tensors). The logarithmic principal stretches ϵ_i, which are physically meaningful and measurable quantities, are related to θ_i as $\epsilon_i = \frac{1}{2}\log\theta_i$. Integrating Eq. (56) in its principal form over the time step dt with integration limits $(t^n, \epsilon_i^{\mathrm{e},tr})$ and $(t^{n+1}, \epsilon_i^{\mathrm{e},n+1})$ gives us the corrected values,

$$\epsilon_i^{\mathrm{e},n+1} = \epsilon_i^{\mathrm{e},tr} - d\lambda\cdot\frac{\partial g_p}{\partial\tau_i'}\bigg|^{n+1}, \quad i = 1,2,3, \tag{57}$$

where $d\lambda$ is calculated using the discrete consistency condition $f_p^{n+1} = 0$. $\boldsymbol{b}^{\mathrm{e},n+1}$ and $\boldsymbol{\tau}'^{,n+1}$ are now updated. The plastic mass is updated as [38],

$$M^{\mathrm{p},n+1} = M^{\mathrm{p},tr} + b\rho_f^0\log\left(\frac{J^{n+1}J^{\mathrm{e},n}}{J^{\mathrm{e},n+1}J^n}\right) \tag{58}$$

The updated stress is used to re-evaluate the yield condition, which determines whether an additional iteration of the predictor-corrector scheme is necessary.

Large displacement/rotation–small strain Next, we describe the model for large displacements/large rotations, but small strains [53]. This may be more appropriate for laterally extensive (large aspect ratio) reservoirs and some ductile rocks deforming under the well operation. Here, the small strain feature can be exploited to replace the iterative predictor–corrector scheme with analytical expressions for the plastic multiplier and the elastoplastic stress, which change within the Newton loop of the mechanics solver. This provides computational efficiency. From Eq. (40), the volumetric and deviatoric parts of the plastic strain tensor are

$$d\varepsilon_v^{\mathrm{p}} = \alpha_g d\lambda, \quad \boldsymbol{de}^{\mathrm{p}} = d\lambda\frac{1}{2\sqrt{J_2^{n+1}}}\boldsymbol{s}^{n+1}, \tag{59}$$

and Eq. (40) provides the incremental fluid mass due to plastic strain as

$$dM^{\mathrm{p}} = \rho_f^0\alpha_g\beta d\lambda \tag{60}$$

Given the plastic yielding at t^{n+1}, we need to update the elastoplastic stress. First, we obtain an explicit algebraic expression for the plastic multiplier. Using the volumetric-deviatoric stress split from Eq. (17) and the incremental form in Eq. (49), we write:

$$\begin{aligned}\boldsymbol{s}^{n+1} &= 2G\left(\boldsymbol{dE}_d - \boldsymbol{de}^{\mathrm{p}}\right) + \boldsymbol{s}^n\\ S_v^{n+1} &= K_{dr}\left(dE_v - d\varepsilon_v^{\mathrm{p}}\right) - bdP_e + S_v^n\end{aligned} \tag{61}$$

Substituting Eq. (59) into Eq. (61),

$$\left(1 + \frac{Gd\lambda}{\sqrt{J_2^{n+1}}}\right)\boldsymbol{s}^{n+1} = 2G\boldsymbol{dE}_d + \boldsymbol{s}^n, \tag{62}$$

$$S_v^{n+1} = K_{dr}\left(dE_v - \alpha_g d\lambda\right) - b\left(P_e^{n+1} - P_e^n\right) + S_v^n. \tag{63}$$

Taking the scalar product of both sides of Eq. (62),

$$\left(1+\frac{G d\lambda}{\sqrt{J_2^{n+1}}}\right)^2 \boldsymbol{s}^{n+1}:\boldsymbol{s}^{n+1} = 4G^2\boldsymbol{dE}_d:\boldsymbol{dE}_d + 4G\boldsymbol{s}^n:\boldsymbol{dE}_d + \boldsymbol{s}^n:\boldsymbol{s}^n \tag{64}$$

Using the definition of J_2^{n+1} and J_2^n,

$$\left(d\lambda+\frac{\sqrt{J_2^{n+1}}}{G}\right)^2 = 2\boldsymbol{dE}_d:\boldsymbol{dE}_d + \frac{2}{G}\boldsymbol{s}^n:\boldsymbol{dE}_d + \frac{J_2^n}{G^2}. \tag{65}$$

Defining the right hand side of the above equation as $(r^{n+1})^2$, we obtain the plastic multiplier as

$$d\lambda = r^{n+1} - \frac{\sqrt{J_2^{n+1}}}{G} \tag{66}$$

Substituting S_v^{n+1} from Eq. (63) and J_2^{n+1} from Eq. (66) in the discrete consistency condition $f_p^{n+1}=0$ provides us the final expression for the plastic multiplier

$$d\lambda = \frac{\alpha_f\left(K_{dr}dE_v + P_e^{n+1}(\beta-b) + S_v^n + bP_e^n\right) + r^{n+1}G - \gamma}{K_{dr}\alpha_f\alpha_g + G}. \tag{67}$$

Assuming $\beta = b$ means the role of pore pressure is limited to knowing the effective stress at nth time step, $S_v^n + bP_e^n$. Once we have the plastic multiplier, we calculate the stress and strain as follows. Substituting J_2^{n+1} from Eq. (66) into Eq. (59) results in

$$\boldsymbol{s}^{n+1} = \boldsymbol{de}^{\mathrm{p}}\,\frac{2G(r^{n+1}-d\lambda)}{d\lambda}, \tag{68}$$

which when substituted into Eq. (62) gives us the expression for the deviatoric plastic strain increment

$$\boldsymbol{de}^{\mathrm{p}} = \frac{d\lambda}{r^{n+1}}\left(\boldsymbol{de}+\frac{\boldsymbol{s}^n}{2G}\right) \tag{69}$$

$d\varepsilon_v^{\mathrm{p}}$ can be updated using Eq. (59) and S_v can be updated using Eq. (63) (recall that P_e^{n+1} is available from the solution of the flow problem at the current sequential iteration). For large positive values of S_v, e.g. when the rock is under tension such as during hydraulic fracturing, $d\lambda$ can be too large making it difficult to project the stress back to the yield surface. In fact, if $d\lambda > r^{n+1}$, then Eq. (66) implies $\sqrt{J_2^{n+1}} < 0$, which is not physical. We address this issue by calculating $d\lambda$ as the minimum of r^{n+1} (equivalent to assuming $J_2^{n+1}=0$) and the value obtained by Eq. (67).

3.2.2. Fault slip model

The fault tractions $\boldsymbol{L_f}$ are additionally constrained by the M-C slip condition, Eq. (21). When the condition is violated at a fault node, the fault slip $\boldsymbol{D}_f$ is incremented. This is achieved by solving the mechanics problem in a loop:

1. The system of equations Eq. (53) is solved, which accounts for the nonlinearities due to finite strain and plasticity, as described above.
2. The fault tractions $\boldsymbol{L}_f^{(k)}$ are used to check the slip condition Eq. (21) and perturbation to the tractions are calculated for the fault nodes violating the condition.
3. Two local equilibrium equations, extracted from the top row of Eq. (53), are solved at positive and negative side fault nodes to calculate adjustment in $\boldsymbol{U}^{+,(k)}$ and $\boldsymbol{U}^{-,(k)}$ corresponding to the traction perturbations. The local equilibrium equations are smaller in size than the global system and hence solved using a direct solver.
4. Adjustments in the displacements are used in Eq. (8) to compute the slip increment.
5. If the slip increment is below a threshold, exit the loop. Otherwise, go back to step 1 above with the updated slip in $\boldsymbol{R}_l$.

See Eqs. (76)-(78) in [16] for the detailed algorithm. Our framework is also capable to model fault gouge zone. This will require choosing the thickness of fault gauge zone and assign different friction angle, dilation angle and cohesion to the gauge zone cells from other grid cells.

3.3. Flow model

The global mass conservation statements for oil and water (Eq. (48)) phases are written for each element in the mesh. The surface integral term with outward normal flux $\overline{W}$ becomes a summation of outward normal fluxes over all the faces of an element. The discrete flux $\overline{W}_{ij}$ for face ij between element i and element j is approximated using a nonlinear two-point flux approximation (TPFA) [64], which expresses the flux in terms of the element pressures P_i and P_j, the face transmissibility, and the fluid phase mobility $\rho_N k_{rN}/\mu_N$. The face transmissibility depends on the permeabilities $\boldsymbol{k}_i$ and $\boldsymbol{k}_j$, element sizes, angles between the face normal vector and the vector connecting the element barycenters as well as on the pressures of the neighboring elements. The dependence on pressure renders the flux approximation scheme nonlinear and applicable to the full tensor permeability field that arises during a finite strain simulation, even when the initial permeability field is isotropic.

The flow problem is nonlinear due to pressure-dependent fluid compressibility and viscosity and, in case of multiphase flow, saturation-dependent relative permeability and capillary pressure relations. We use Newton's method to linearize the flow problem in terms of the vector of element-centered pressure and saturation increments. For two-phase oil-water system, denoting the oil pressure increment as dP_o and the water saturation increment as dS_w, the linear system is

$$\begin{bmatrix} \frac{\partial \boldsymbol{R}_o}{\partial \boldsymbol{P}_o} & \frac{\partial \boldsymbol{R}_o}{\partial \boldsymbol{S}_w} \\ \frac{\partial \boldsymbol{R}_w}{\partial \boldsymbol{P}_o} & \frac{\partial \boldsymbol{R}_w}{\partial \boldsymbol{S}_w} \end{bmatrix}^{(k)} \begin{bmatrix} \boldsymbol{dP}_o \\ \boldsymbol{dS}_w \end{bmatrix}^{(k)} = - \begin{bmatrix} \boldsymbol{R}_o \\ \boldsymbol{R}_w \end{bmatrix}^{(k)}, \tag{70}$$

where k is the Newton iteration counter. See [16] for details. Nonlinear TPFA gives rise to pressure-dependent transmissibilities, as mentioned above. We assume the transmissibilities to be frozen within a time step, which introduces sparsity in the Jacobian matrix of Eq. (70) at the cost of a small reduction in the convergence rate. Following the sequential iterative solution scheme mentioned earlier, we freeze the incremental total volumetric stress (dS_v) and the incremental volumetric plastic strain ($d\varepsilon_v^{\mathrm{p}}$) to their respective values at the previous sequential iteration. Therefore, their contributions to the Jacobian matrix blocks is zero.

3.4. Sequential iterative solution strategy

Given the solutions at time step n, we use a sequential iterative scheme to solve the coupled flow-geomechanics problem at time step $n+1$. This approach, which is similar to our approach in the infinitesimal strain model [16], is as follows. At sequential iteration $s+1$ of time step $n+1$, we solve the discrete flow system for element-centered pressures and saturations ($P_o^{n+1,s+1}$, $S_w^{n+1,s+1}$) using Newton's method, while fixing $dS_v = S_v^{n+1,s} - S_v^n$ and $d\varepsilon_v^{\mathrm{p}} = \varepsilon_v^{\mathrm{p},n+1,s} - \varepsilon_v^{\mathrm{p},n}$. We use a block GMRES solver with Block Incomplete LU (BILU) preconditioner to solve the system. Next, we solve the discrete mechanical system for nodal displacement d.o.f. $\boldsymbol{U}^{n+1,s+1}$, element-averaged internal variables $\varepsilon_v^{\mathrm{p},n+1,s+1}$ and $M^{\mathrm{p},n+1,s+1}$, and fault-nodal traction d.o.f. $\boldsymbol{L}_f^{n+1,s+1}$ and slip d.o.f. $\boldsymbol{D}_f^{n+1,s+1}$ while assuming that the flow solution is fixed at ($P_o^{n+1,s+1}$, $S_w^{n+1,s+1}$). The mechanics problem is strongly nonlinear. The nonlinearity due to finite strain and plasticity is addressed via Newton's method and an iterative return mapping algorithm in case of large strains, and the nonlinearity due to fault slip is addressed via an inner loop over the mechanics problem. We use PETSc's field split AMG preconditioner with a GMRES linear solver [62, 65]. Convergence of the entire solution is checked by comparing the norm of the solutions at s and $s+1$ iterations. If not converged, the sequential loop continues for another iteration over the two solvers–flow and geomechanics–until a converged solution, ($\boldsymbol{U}^{n+1}$, $\boldsymbol{L}_f^{n+1}$, $\boldsymbol{D}_f^{n+1}$, P_o^{n+1}, S_w^{n+1}), is achieved [16]. Depending on the strength of coupling between the flow and mechanical processes and the strength of nonlinearities within each problem, the number of sequential iterations required for convergence at a time step varies with time.

Algorithm 1: Sequential iterative solution strategy.

```
Result: Pressure, saturation, stress, strain and displacement
Initialization
while time step n < N do
    Sequential counter s = 0
    while Not converged do
        s = s + 1
        Solve flow problem Eq. (70)
        Solve mechanics problem Eq. (53)
        if f_p^tr ≤ 0 then
            Compute plastic strain tensor
        else
            Continue
        end
    end
end
```

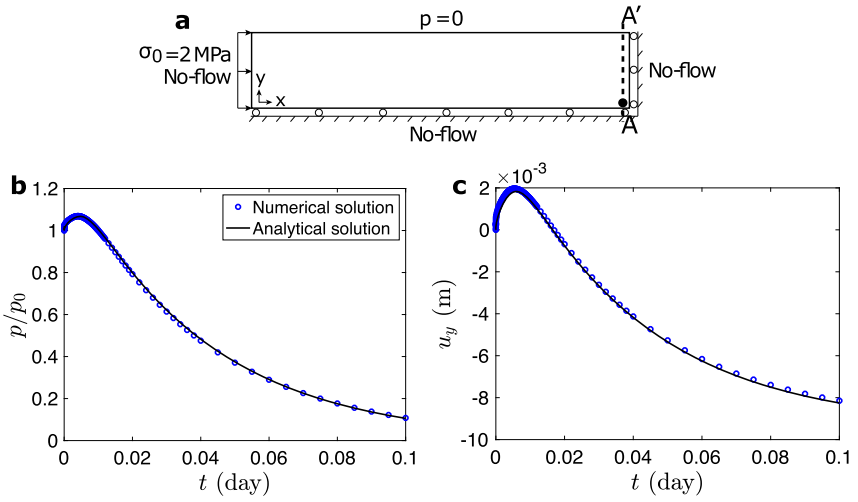

Fig. 3. The Mandel problem. (a) Model geometry with boundary conditions. The observation point A is shown in a black circle. The observation line A'A is shown in dash line. (b) Comparison of dimensionless pressure vs. time from the numerical simulation and analytical solution. (c) Comparison of displacement vs. time from the numerical simulation and analytical solution.

4. Representative numerical simulations

We verify our numerical framework and its implementation by simulating the Mandel and the rigid footing consolidation problems. Then we simulate production-induced fault slip in an oil reservoir to answer the questions posed in the beginning, (1) how plasticity affects the onset time, location and magnitude of slip events, and (2) how rock's elastic moduli affect this coupling.

4.1. The Mandel problem

We solve Mandel's biaxial consolidation problem to test the accuracy of the mechanics-to-flow coupling in our coupled geomechanics simulator. See the model in Fig. 3a. A uniform and constant compression of 2 MPa is applied on the left boundary of the model. The right and bottom boundaries are fixed and no-flow, while the top boundary is a traction-free drained boundary with the excess pressure set at p=0. We choose the following model properties: model dimensions $L_x \times L_y$ = 50 × 10 m^2, compression 2 MPa, drained Young's modulus $E = 100$ MPa, drained Poisson ratio $\nu = 0.3$, Biot coefficient $b = 0.9$, initial porosity $\phi(t = 0) = 0.2$, initial permeability $k = 9.869 \times 10^{-14}$ m^2, and fluid viscosity $\mu = 1$ cp. We can express these moduli in terms of the moduli used in the numerical model above: $E = 9K_{dr}G/(3K_{dr} + G)$ and $\nu = (3K_{dr} - 2G)/(2(3K_{dr} + G))$. We select the point near the right bottom corner as our observation point to investigate the evolution of pressure and displacement with time (Fig. 3b, c). In the Mandel problem, the flow and mechanics processes are two-way coupled to each other and the mechanics-to-flow coupling leads to the well-known Mandel-Cryer effect [66] where the pore pressure (Fig. 3b) and the vertical displacement (Fig. 3c), away from the drained boundary, rise at early times, before continuing to decline due to drainage.

To understand the effect of plasticity, we conduct two simulations with two different material models: a Drucker-Prager (DP) material and an elastic (EL) material. Material properties are as follows: drained Young's modulus $E = 100$ MPa, drained Poisson's ratio $\nu = 0.3$, Biot's coefficient $b = 0.9$, α_f and α_g = 0.0562, $\gamma = 1.5$ MPa. We plot the evolution of vertical stress, strain, and stress invariants in Fig. 4, and the evolution of vertical displacement and pressure in Fig. 5. During early times, both the total compressive stress and the pore pressure rise due to the Mandel-Cryer effect. The first invariant I_1' is nearly constant at 4 MPa as the second invariant $\sqrt{J_2}$ is rising from 1.15 to 1.27 MPa. Fig. 5a and b also show that the deformation and pressure evolve almost identically during early times. During intermediate times, once the pressure depletion effect of drainage reaches the observation point, I_1' starts to decrease faster. $\sqrt{J_2}$ continues to increase throughout the drainage. When the plastic yield criterion is satisfied (stress path touching the straight blue line), plastic flow begins and the material deforms along the yield line as long as the deviatoric stresses are large enough. Plastic strain begins and the total strain is larger in the plastic simulation compared to the elastic simulation. Plastic dilatancy leads to a higher consolidation (higher u_y) and a lower excess pressure in the plastic material compared to the elastic material (Fig. 5), which agrees with the observations reported in literature [38]. At later times, the stress state returns to the elastic region (below the yield line Fig. 4c) because I_1' decreases faster due to pressure depletion than the rate of increase in $\sqrt{J_2}$.

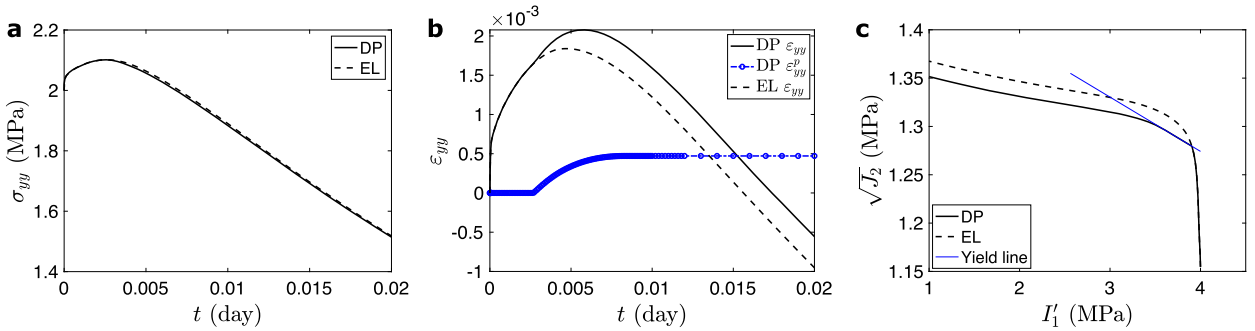

Fig. 4. Time evolution of the (a) vertical stress, (b) vertical strain and (c) evolution of the stress state at the observation point *A* in Fig. 3a. Vertical plastic strain (blue dot line) starts to increase and the elastic simulation (EL, dash line) shows higher vertical stress and lower vertical strain than Drucker-Prager plastic simulation (DP, solid line) after stresses reach the yield line (blue line). (For interpretation of the colors in the figure(s), the reader is referred to the web version of this article.)

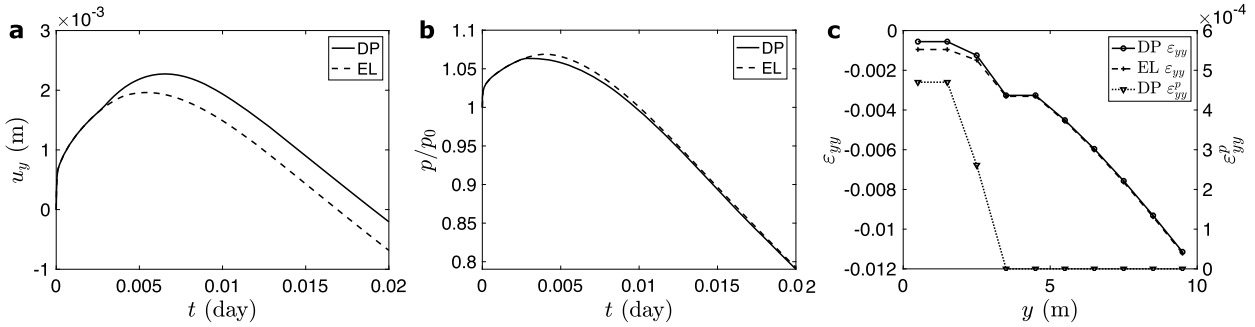

Fig. 5. Time evolution of (a) vertical displacement and (b) dimensionless pressure at the observation point *A*. Elastic simulation (EL, dash line) shows lower vertical displacement and higher pressure than Drucker-Prager plastic simulation (DP, solid line) after plastic failure initiates. (c) Profile of vertical strain along AA' at t=0.02 day. Vertical strain decreases from point A to A'. Total vertical strain from DP simulation (solid line) is higher than that from EL simulation (dash line) in the cells that have plastic failure (dot line).

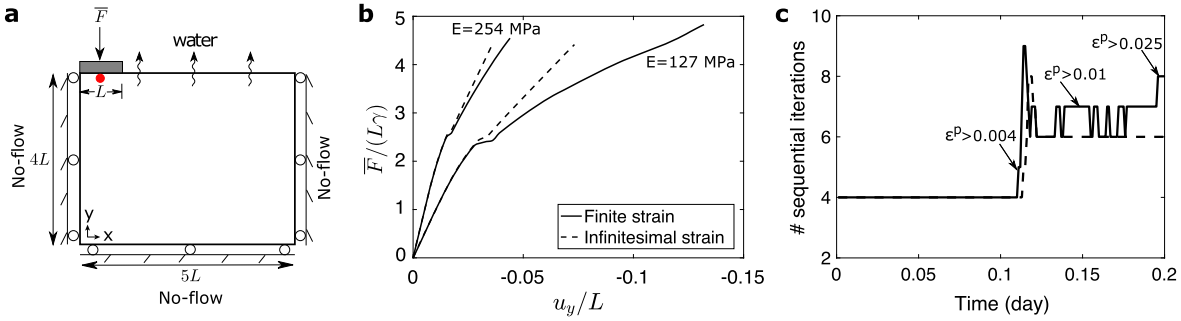

Fig. 6. The rigid footing problem. (a) Model geometry with boundary conditions. The observation point, shown as a red dot, is below the footing. (b) Comparison of finite strain and infinitesimal strain simulations for two types of rocks: weak ($E = 127$ MPa) and strong ($E = 254$ MPa). (c) Number of sequential iterations for convergence between flow and mechanics problems in finite and infinitesimal strain simulations for strong rock ($E = 254$ MPa).

4.2. The rigid footing problem

The problem deals with a water-saturated rock layer subjected to a strip footing load on the top boundary that increases with time. Because of the axisymmetry of the problem, we only need to consider the right half of the domain (Fig. 6a). All the boundaries are set to no-flow boundaries except the top boundary, which allows water to drain as the layer compacts. A load $\overline{F}$ (Newton per meter) that increases in time at a constant rate is applied over the footing length L. Model properties are as follows: $L = 5$ m, compression increases from 0 with a loading rate of 165 Pa/sec, drained Poisson's ratio $\nu = 0.3$, Biot coefficient $b = 1$, initial porosity $\phi(t = 0) = 0.2$, homogeneous isotropic initial permeability ($\boldsymbol{k}(t = 0) = k\mathbf{1}$) with $k = 9.869 \times 10^{-13}$ m^2 (1 darcy), fluid viscosity $\mu_w = 1$ cp, friction angle of 30 degree, dilation angle of 0, and $\gamma = 0.127$ MPa. The model has 40×50 mesh elements. We select a point below the top boundary as our observation point where we plot compression versus displacement (Fig. 6b).

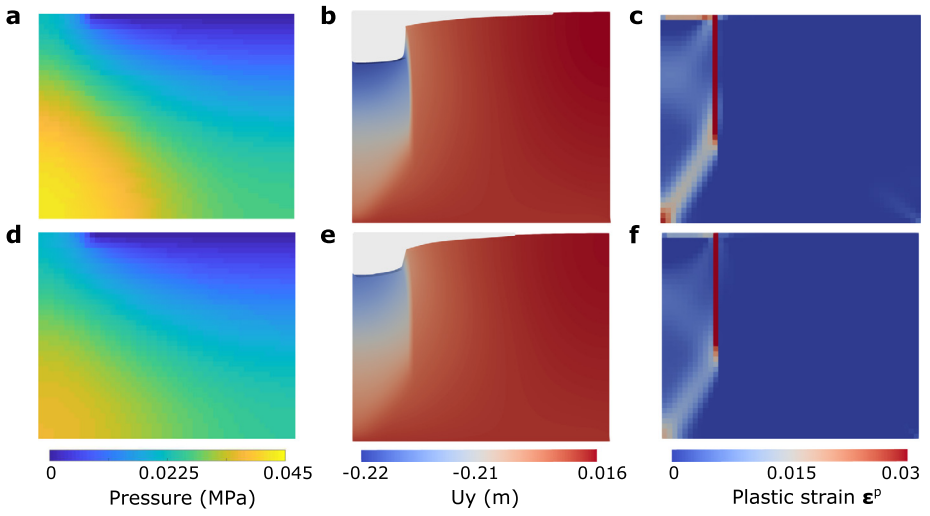

Fig. 7. Results from finite strain (a to c) and infinitesimal strain (d to f) simulations. (a) Overpressure, (b) vertical displacement (exaggerated by a factor of 20), and (c) plastic strain magnitude at $t = 0.2$ day.

Using the same model, we compare the results from finite strain and infinitesimal strain simulations for two types of rocks: weak ($E = 127$ MPa) and strong ($E = 254$ MPa), while keeping other parameters the same. Deformation is smaller in the stiffer rock, as shown in Fig. 6b. The larger consolidation experienced by the weaker rock is correctly modeled in the finite strain simulation compared to the infinitesimal strain, a result that agrees with literature (see Fig. 10 in [67] and Fig. 10 in [45]). For the same footing load, the compaction is larger in the finite strain simulation. Also, the difference between finite and infinitesimal curves increases as the consolidation process continues. In Fig. 6c, we show the difference between the number of sequential iterations for convergence between flow and mechanics problems in the finite and infinitesimal strain simulations. As the plastic strain magnitude increases, both simulations need more iterations to converge. Since the plastic deformation is delayed in the infinitesimal strain model, its number of iterations lag behind that of the finite strain model.

We plot the spatial profiles of pressure, displacement and plastic strain magnitude from finite strain and infinitesimal strain simulations for the case with strong ($E = 254$ MPa) rock as shown in Fig. 7. Pressure increases under compression except the drained top boundary where pressure remains unchanged. We observe negative displacement u_y in the area under compression and smaller positive displacement in other area. Plastic failure initiates on the compression boundary and propagates downwards. The border between the compression boundary and the flow boundary has the highest plastic strain because of high S_{xy} in the finite strain simulation or σ_{xy} in the infinitesimal strain simulation. This serves as a barrier and creates a failure zone. The comparison between finite strain and infinitesimal strain simulations shows that the finite strain model can capture the higher overpressure, larger displacement and plastic strain magnitude resulting from the footing load in this case.

4.3. Production-induced plastic failure and fault slip

Motivated by the setup in Fig. 1, we create a 3D geomechanical model of a reservoir-caprock-basement system (Fig. 8) with a sealing fault in the normal faulting stress regime. The model dimensions are 2 km $\times$ 2 km $\times$ 2 km in x, y and z directions. The depth interval of the model is from $z = 0.5$ km to $z = 2.5$ km below the ground surface. A dome-shaped reservoir is located at the center of the model with an average thickness of 160 m. The fault is located east of the model center with a dip angle of 80°, and the fault strikes north-south. We have one well near the top of the reservoir dome producing oil from the top three layers of the reservoir.

The model is initialized under mechanical and hydrostatic equilibrium with a normal faulting stress regime. We apply a lateral compression on the east boundary (x-positive surface) which is 70% of the overburden to create a normal faulting stress regime. Both the compression and overburden increase linearly with the lithostatic gradient. Initial stresses are in equilibrium with the gravitational and boundary stresses such that the initial displacement is zero. All boundaries are no-flux boundaries. The reservoir is initially saturated with 12% water and 88% oil. The initial reservoir pressure is around 2075 psi. We use the linear slip-weakening friction model to describe quasi-static frictional failure on the fault. The friction coefficient decreases from a static value $\mu_s = 0.5$ to a dynamic value $\mu_d = 0.2$ as the slip magnitude increases from zero to the critical slip distance $d_c = 0.1$ m. The value of d_c falls within the range of critical slip weakening distance reported in multiple studies [68–71]. We use a D-P perfectly plastic model where the yield surface touches the outer vertices of the M-C model, i.e. the inscribed D-P model. We use a friction angle of $\phi_f = 20$ degree, dilatation angle of $\phi_g = 20$ degree, and cohesion of $c = 1$ MPa [72]. See the appendix for the relations between $(\alpha_f, \alpha_g, \gamma)$ and (ϕ_f, ϕ_g, c). To simulate a gouge

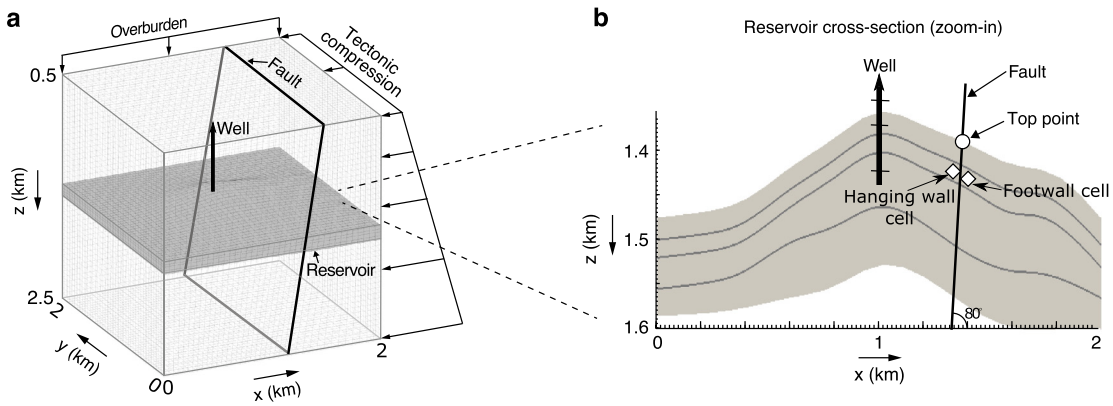

Fig. 8. (a) Physical model with a well producing from a reservoir (gray color) confined between caprock and basement (white color) and intersected by a fault. (b) A vertical cross section of the reservoir showing the layered topography, well and fault. Positions of the Top point, Hanging wall cell, and Footwall cell, where detailed analysis of stress and slip will be carried out in the Results section, are shown.

Table 1
Input parameters.

Parameters	Value
Bulk density, ρ_s (kg/m^3)	2460
Oil density at surface conditions, ρ_o (kg/m^3)	806.26
Water density at surface conditions, ρ_w (kg/m^3)	1000.0
Water viscosity at reservoir conditions, μ_w (cp)	0.4
Biot coefficient, b	0.8
Reservoir permeability (md)	5
Caprock permeability (md)	0.0001
Fault permeability (md)	0.0001
Initial Eulerian porosity, ϕ	0.1
Static coefficient of friction, μ_s	0.5
Dynamic coefficient of friction, μ_d	0.2
Critical slip distance, d_c (m)	0.1
Fault cohesive strength (kPa)	0
Friction angle (degree)	20
Dilation angle (degree)	20
Cohesion (MPa)	1
Poisson's ratio	0.25
Initial horizontal-to-vertical total stress ratio, r_{tec}	0.7
Well perforation top coordinates (x, y, z) (m)	(949.4, 971.3, 1376.7)
Well perforation bottom coordinates (x, y, z) (m)	(941.1, 972.2, 1440.6)
Number of grid cells in the x-direction, N_x	39
Number of grid cells in the y-direction, N_z	40
Number of grid cells in the z-direction, N_z	43
Average grid cell size (m)	50

zone, we can assign different friction angle, dilation angle and cohesion to the cells adjacent to fault. The model is populated with homogeneous isotropic properties given in Table 1. The overburden and underburden are hydraulically isolated from the reservoir. Transmissibilities of the fault in the three directions (lateral shear, dip shear, and normal directions) are set to zero. The oil relative permeability in presence of water k_{ro}, the oil formation volume factor B_o, and the oil viscosity μ_o are plotted as saturation- and pressure-dependent functions in Fig. 9. The formation volume factor is defined as the ratio of the fluid density at the atmospheric pressure to the fluid density at reservoir pressure. B_o is related to the oil compressibility as $c_o = -(1/B_o)dB_o/dp_o$.

We consider four cases (listed in Table 2) by varying geomechanical properties such as the drained Young's modulus E and bulk modulus K_{dr}. We produce oil at 2000 bbl/day (318 m^3/day) for 850 days in the four cases. For each case, we run finite strain and infinitesimal strain simulations. To understand the effect of rock type on fault slip and plastic failure, we compare the spatial profiles and time evolution of reservoir pressure, vertical displacement, plastic magnitude and slip area in four cases. The slip area is important because it determines the seismic event magnitude as per Eq. (10). We analyze the stress path at different locations: the hanging wall cell, the footwall cell and the fault top point as shown in Fig. 8 to identify the effect of plastic failure on fault slip. We also analyze the stress path in the four cases to understand the rock stiffness-induced temporal complexity of plastic failure and fault activation process.

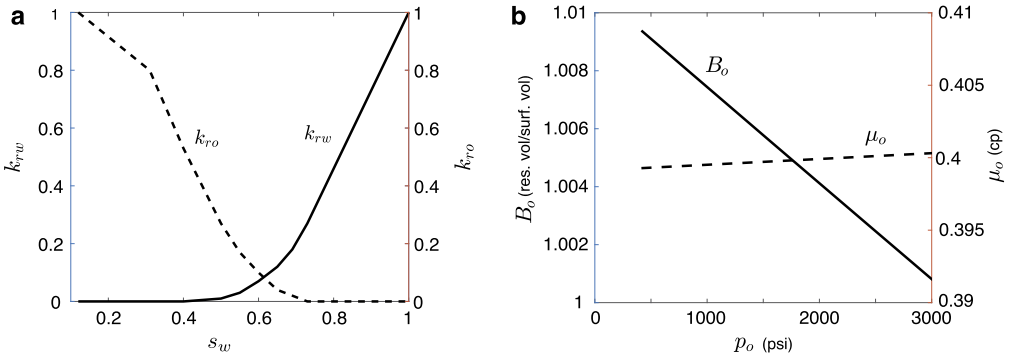

Fig. 9. (a) Relative permeability of water k_{rw} (solid) and relative permeability of oil k_{ro} (dash) as functions of the water saturation s_w. (b) The oil formation volume factor B_o and the oil viscosity μ_o.

Table 2
Four cases of reservoir-caprock system defined in terms of their elastic moduli.

		E (GPa)	K_{dr} (GPa)
Case 1	Overburden and underburden	26.4	17.6
	Reservoir	26.4	17.6
Case 2	Overburden and underburden	26.4	17.6
	Reservoir	12.9	8.6
Case 3	Overburden and underburden	12.9	8.6
	Reservoir	26.4	17.6
Case 4	Overburden and underburden	12.9	17.6
	Reservoir	5.3	3.6

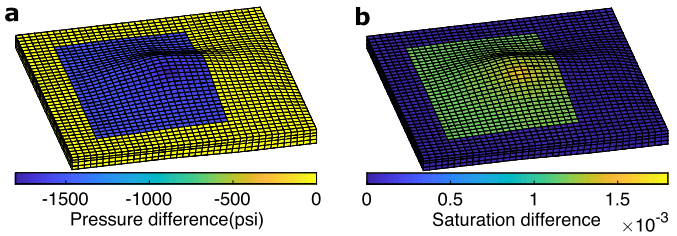

Fig. 10. 3D fields of (a) pressure change and (b) water saturation change at day 850. Pressure change is almost zero (yellow color) in the footwall block due to the low permeability of the fault. Water saturation increases slightly due to oil production.

4.3.1. Spatial profiles and time evolution

We plot 3D fields of Case 1 results at $t = 850$ day from the finite strain elastoplastic simulation in Fig. 10 and Fig. 11. Due to production, the reservoir pressure decreases and the water saturation increases near the well and propagates to the hanging wall side of the reservoir. Because of the impermeable fault, pressure and water saturation remain unchanged on the footwall side. The pressure remains almost constant in caprock and basement because they are hydraulically isolated from the reservoir.

To understand the geomechanical signatures of reservoir pressure depletion, we plot vertical displacement of the whole field in Fig. 11a. Pressure depletion leads to volumetric contraction of the reservoir and causes negative vertical displacements above the reservoir and positive displacement below the reservoir. The maximum downward displacement decreases from 3 cm above the reservoir to 1.2 cm on the top surface.

We examine the evolution in the stress vs. average reservoir pressure space of the footwall block cell, where plastic failure initiates, and it's corresponding hanging wall block cell in Fig. 12. Production-induced reservoir contraction leads to negative normal stresses for the hanging wall block cells. However, for the footwall block cells, reservoir contraction in the hanging wall block applies pull in the x direction and leads to an increase in S'_{xx}. In y and z directions, footwall block cells experience smaller contraction than hanging wall block cells so S'_{yy} and S'_{zz} decrease slightly. The combination of normal stress changes causes a rapid decrease in effective volumetric stress for hanging wall block cells, and a small decrease in effective volumetric stress for footwall block cells (Fig. 12d). Reservoir contraction increases the shear stress magnitude in both hanging wall and footwall blocks as shown in Fig. 12c. The deviatoric stress invariant is dominated by changes in the normal stresses. The increase in S'_{xx} overcomes the decrease in S'_{yy} and S'_{zz} and leads to a large increase in the deviatoric stress in the footwall block. However, for hanging wall block cells, the decrease in S'_{xx} balances out with the decrease in S'_{yy}

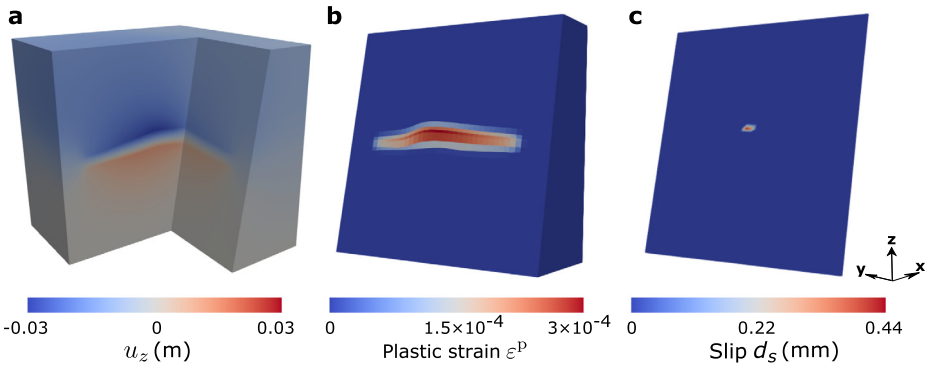

Fig. 11. 3D fields of (a) vertical displacement, (b) plastic strain magnitude in the footwall block, and (c) slip magnitude on the fault surface at day 850. (a) shows a cut-away view of the u_z field using a slice along the fault surface and a $y = 1000$ m slice. See videos in the supplementary material.

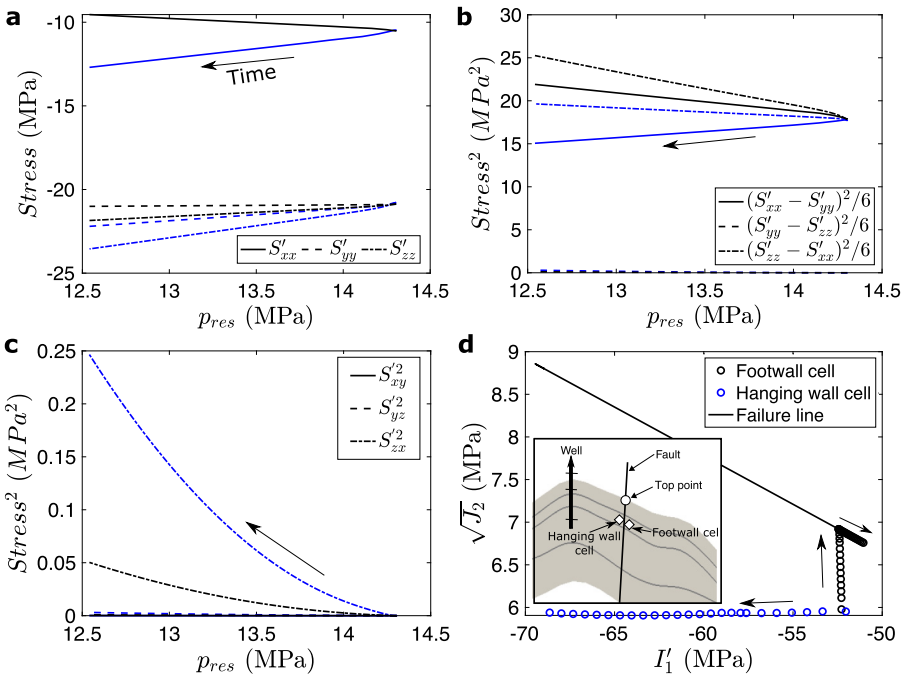

Fig. 12. Case 1: Stress evolution. (a) Effective normal stresses (b) and (c) deviatoric stresses versus pressure for the footwall block cell (black line) and it's corresponding hanging wall block cell (blue line). (d) Stress paths of the footwall block cell (black points) and hanging wall block cell (blue points) in the stress invariant space.

and S'_{zz} and the deviatoric stress remains almost unchanged (Fig. 12b and d). Thus, plastic failure initiates in the footwall block and propagates laterally and vertically. The plastic strain magnitude in the footwall block is plotted in Fig. 11b.

Reservoir contraction also applies downward pull on the reservoir top surface and upward pull on the reservoir bottom surface. This is production-induced shear. Since the boundary conditions in Fig. 8(a) are such that all points on the fault experience downdip tectonic shear, both the production-induced shear and the tectonic shear are acting downdip on the top surface. As a result, one of the points on the reservoir top is most likely to slip compared to all other locations on the fault. This is confirmed by Fig. 11c which shows that the slip nucleates near the top of reservoir.

To compare the results among finite strain and infinitesimal strain simulations, we keep the pressure drop, which is the driving force behind induced seismicity, the same between the two simulations (Fig. 13a). The distributions of displacement, plastic strain and fault slip remain similar in both cases to Fig. 11, which implies that finite strain plasticity did not impact the location of the hypocenter. However, the magnitudes of these quantities are different in the two simulations which implies that the seismic/aseismic slip onset time and the magnitude are different. This is an important result that can explain why some of the induced seismicity simulation models, which assume infinitesimal strain over decade-long production from a oil/gas reservoir or injection in an aquifer, under- or over-estimate the timing and magnitude of induced events. Compared with the finite strain simulation, as shown in Fig. 13, the vertical displacement in the infinitesimal simulation is smaller for the same amount of pressure drop because of a lack of plastic yielding. In the infinitesimal simulation, compared to the

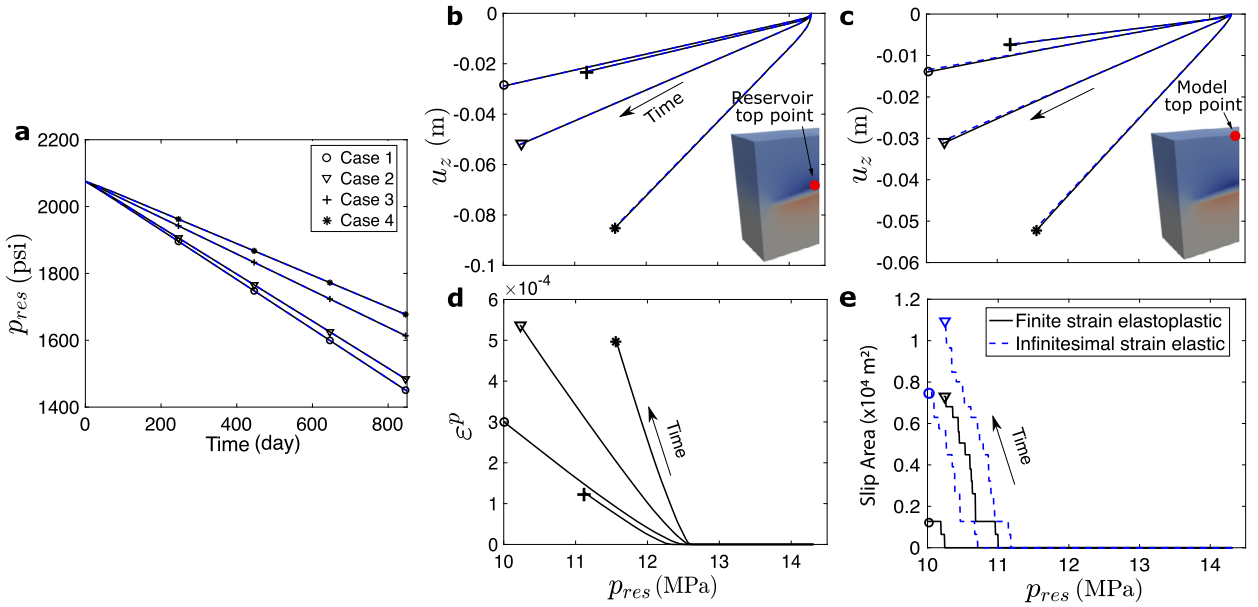

Fig. 13. Time evolution of (a) the average reservoir pressure. Evolution of (b) the vertical displacement at the top of the reservoir and (c) at the top of the model, (d) plastic strain magnitude at the footwall block cell, and (c) slip area on the fault surface versus the average reservoir pressure for the four cases with finite strain and infinitesimal strain simulations. See video of (b) in the supplementary material.

finite strain elastoplastic simulation, the fault slips earlier, at a smaller pressure drop value, and generate a larger slip area (larger M_w) at the end of production.

With different rock types, we observe spatial distributions of pressure, saturation, displacement, plastic strain and fault slip that are similar to Fig. 11. However, the time evolutions are different and revealing. With the same amount of oil produced, when the reservoir rock has a smaller bulk modulus and Young's modulus, we observe less reservoir pressure drop in Case 2 and Case 4 compared to Case 1 (Fig. 13a). When the overburden and underburden rocks have smaller bulk and Young's moduli compared to those of the reservoir (Fig. 13b Case 3), the reservoir pressure drop is again smaller. To identify the effects of pressure depletion on geomechanical behavior, we plot the evolution of vertical displacement and plastic strain magnitude of selected points as well as the fault slip area as functions of the average reservoir pressure in Fig. 13b to e. A weaker reservoir with smaller elastic moduli can be compressed more easily. So, with the same amount of pressure decline, we observe larger vertical deformation in Case 2 and Case 4 compared to Case 1 at both the reservoir top and model surfaces. The mechanics-to-flow coupling (stress and strain terms in Eq. (43)) reduces the drop in reservoir pressure during production. This mechanism is also known as the *compaction drive* in petroleum engineering literature [73]. Comparing Case 1 and Case 3 shows interesting results of practical significance. We observe that Case 3 vertical displacement is larger than Case 1 vertical displacement at the reservoir top and smaller than Case 1 vertical displacement at the model top. The reason is as follows. The caprock in Case 3 has a smaller modulus and it deforms more. However, the downward pull on the caprock decreases as we move away from the reservoir top towards the ground surface because the pressure change is localized inside the reservoir and the induced stresses decay rapidly with distance.

With smaller elastic moduli, the plastic failure initiates at a smaller pressure drop as shown in Fig. 13d. The plastic strain magnitude also increases faster in Case 2 and Case 4 compared to Case 1. In Case 3, a larger portion of the pressure depletion-induced stresses is spent in driving caprock and basement deformations, so we observe a delayed onset of plastic failure and a smaller plastic strain magnitude. The fault slips earlier at a smaller pressure drop in Case 2 compared to Case 1. Since the pressure drop is smaller in Case 3 and Case 4, we do not encounter fault slip during the simulation period. The slip is further delayed in Case 3 because caprock and basement rocks are weaker (smaller moduli).

4.3.2. *Effect of plastic failure on fault slip*

To further understand the relationship between plastic failure and fault slip, we show the results from finite and infinitesimal strain simulations for Case 1. We first examine the time evolution in the space of the deviatoric stress invariant $\sqrt{J_2}$ vs. the effective volumetric stress invariant I_1'. We consider the selected footwall block cell. As shown in Fig. 14a (see video in the supplementary material), production-induced compaction leads to negative I_1' in both finite and infinitesimal strain simulations. Before the onset of plastic failure, $\sqrt{J_2}$ increases in the footwall block cell and later reaches the D-P yield surface. In the finite strain simulation, $\sqrt{J_2}$ decreases and I_1' increases (lower compression) after reaching the yield surface. In infinitesimal strain simulation, $\sqrt{J_2}$ continues to increase and I_1' continues to decrease (higher compression).

In Fig. 14b (see video in the supplementary material), we show the time evolution of the hypocenter (Top point on the fault surface) in the space of shear traction (τ here refers to $|\boldsymbol{\tau}_s|$ in Eq. (21)) vs. the effective normal traction (σ_n'). Reservoir

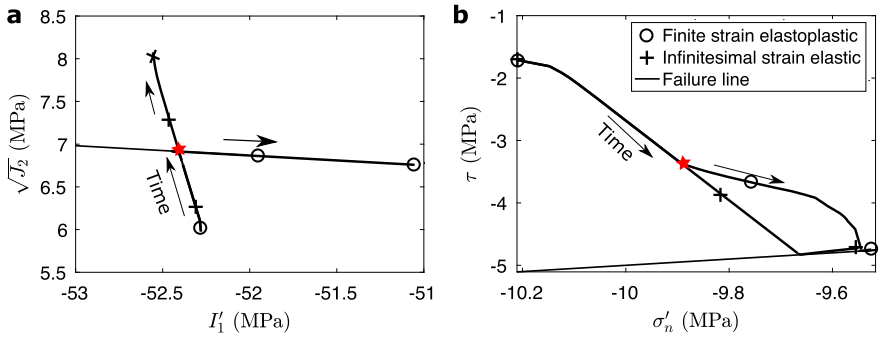

Fig. 14. Stress paths of the (a) footwall block cell and (b) top point on the fault surface from Case 1 finite strain and infinitesimal strain simulations. The solid line in each plot is the M-C failure line. The arrows indicate the direction of time. The red star marks the onset of plastic failure. See videos in the supplementary material.

contraction causes tension on the fault surface which increases σ_n' and causes downdip shear on the Top point which reduces τ. Initially, the stress paths of both elastoplastic and elastic simulations towards the M-C failure line are similar. However, when plastic failure occurs, since plastic failure lowers compression, σ_n' increases rapidly while τ continues to decrease. When plastic failure propagates to the overburden and reservoir boundary, σ_n' increases at a slower rate and τ continues to decrease. This results in a delayed fault slip and a smaller magnitude seismic event in the elastoplastic simulation compared to the elastic simulation.

4.3.3. Effect of rock type

Due to production-induced contraction, induced stresses depend on the pressure drop. We further analyze the evolution of stress as a function of the average reservoir pressure from the finite strain simulation for different rock types at the selected footwall block cell and the fault surface Top point. Initially, the model is under equilibrium with the same initial reservoir pressure and initial I_1' and $\sqrt{J_2}$ in the four cases. Production reduces the reservoir pressure. Before plastic failure begins, production-induced reservoir contraction leads to decrease in I_1' and increase in $\sqrt{J_2}$. As shown in Fig. 15a and b, with the same amount of pressure drop, I_1' decreases less while $\sqrt{J_2}$ increases more when the reservoir has smaller elastic moduli. This leads to a relatively faster growth in the yield function f_p, defined in Eq. (37), for Cases 2 and 4 compared to Case 1, as shown in Fig. 16a. When overburden and basement have smaller moduli, comparing Case 3 and Case 1, the pulling effect due to compaction of the hanging wall reservoir is shared by overburden and basement deformations such that I_1' of the footwall cell decreases faster and $\sqrt{J_2}$ increases slower. The yield function f_p grows relatively slower for Case 3 and it requires additional pressure drop to reach plastic failure, as shown in Fig. 16a.

In the $\sqrt{J_2}$ vs. I_1' space shown in Fig. 17a, as I_1' decreases, $\sqrt{J_2}$ increases faster for cases with smaller reservoir moduli. Since the yield condition requires less $\sqrt{J_2}$ at higher I_1', cases with smaller reservoir moduli tend to fail at a smaller pressure drop. On the other hand, when caprock and basement moduli are smaller, $\sqrt{J_2}$ grows at a smaller rate with decreasing I_1'. This means a larger pressure drop is required to reach the D-P failure line. Reservoir is relatively stable. After plastic failure, stresses stays on the failure line. I_1' increases and $\sqrt{J_2}$ decreases.

We show the evolution of σ_n' and τ as functions of the average reservoir pressure from finite strain simulation for different rock type cases at the Top point in Fig. 15c and d. As pressure drops, contraction-induced tension on the fault surface leads to an increase in σ_n' for the four cases. σ_n' increases slightly faster for cases with smaller reservoir moduli (Case 2 and Case 4) while it grows slower for cases with smaller caprock and basement moduli (Case 3). After plastic failure, σ_n' increases at a higher rate. For Cases 2 and 4, which have smaller reservoir moduli, σ_n' increases faster than Cases 1 and 3. After plastic failure reaches the reservoir top boundary, σ_n' continues to increase with a slower rate in the four cases. Reservoir compression causes downdip shear at the top of the reservoir which leads to a decrease in τ at the reservoir top point. With smaller reservoir moduli, the reservoir contracts more for the same value of pressure drop, the top point experiences larger downdip shear, and τ decreases more as shown in Cases 2 and 4.

We defined the Coulomb Failure Function (CFF) in Eq. (21). In producing reservoirs, the change in τ dominates the evolution of CFF on faults because the fault pressure p_f in σ_n' (Eq. (18)) remains either constant or drops slightly. This is because p_f, during production, is proportional to the pressure on the non-producing side of the fault, so it can correctly predict the slip onset time [16,57]. We observe that for a given pressure drop, CFF grows faster in cases when the elastic moduli of the reservoir rock is smaller. It leads to an earlier onset of slip in Cases 2 and 4 with a smaller pressure drop. On the other hand, when caprock and basement have smaller moduli, both σ_n' and τ show smaller variation for a given drop in the reservoir pressure. Initiation of fault slip requires higher pressure depletion as shown in Fig. 16.

As shown in Fig. 17b, before plastic failure, in the cases where reservoir rocks have smaller moduli, τ decreases faster with increasing σ_n'. Plastic failure leads to a further increase in σ_n'. Because the decrease in τ is larger than the increase in σ_n', Cases 2 and 4 reach M-C line earlier. For weaker caprock and basement rocks, τ decreases at a smaller rate with increasing σ_n'. The fault is relatively stable.

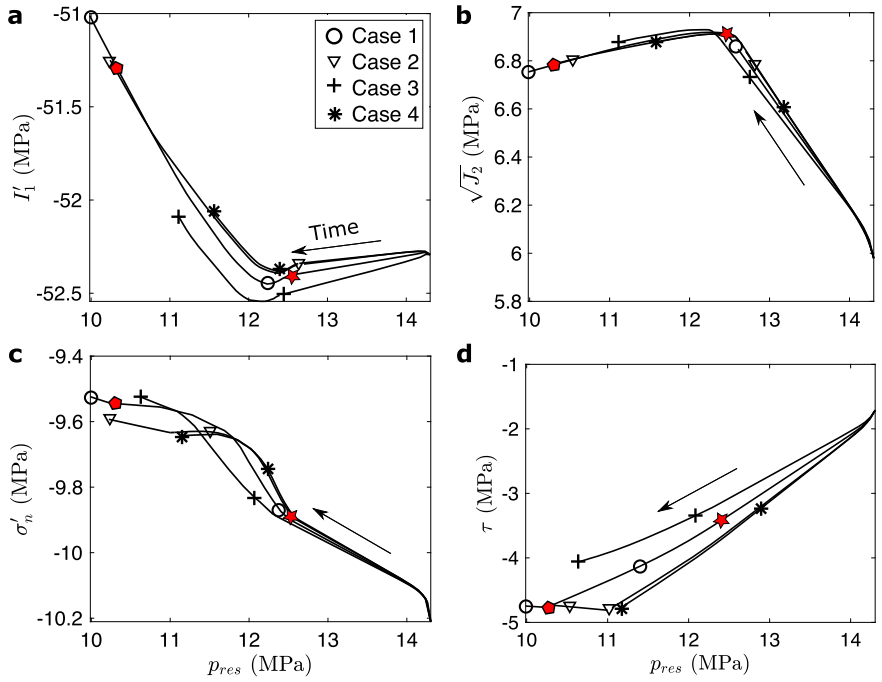

Fig. 15. Effect of rock type on plastic and fault failure. Evolution of (a) effective stress invariant I_1' and (b) deviatoric stress invariant $\sqrt{J_2}$ in the footwall cell, and evolution of (c) effective normal fault traction σ_n' and (d) shear traction τ at the Top point as functions of the average reservoir pressure p_{res} from the four cases in Table 2. The arrows indicate the direction of time. We highlight the initiation of plastic failure with red star and fault slip with red pentagon in Case 1.

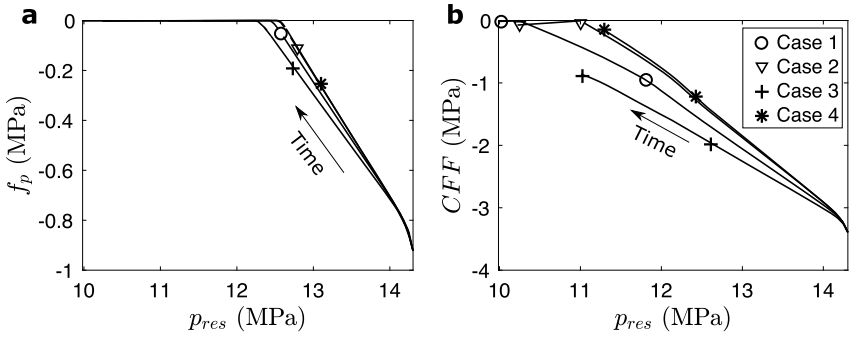

Fig. 16. Effect of rock type on the rate of failure. Evolution of (a) yield function f_p and (b) Coulomb Failure Function CFF, as functions of average reservoir pressure p_{res} from the four cases. The arrows indicate the direction of time.

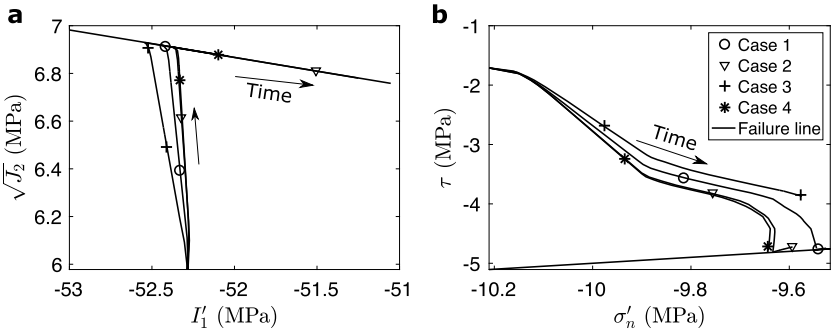

Fig. 17. Stress paths of the (a) footwall block cell and (b) Top point on the fault surface from the four cases. The solid straight line in (a) is the D-P failure line and in (b) is the M-C failure line. The arrows indicate the direction of time. See videos in the supplementary material.

5. Conclusion

We presented a novel simulation framework of coupled multiphase flow, finite strain elastoplasticity and fault slip in petroleum reservoirs. The framework incorporates realistic fault constitutive behavior by using a slip-weakening dynamic friction model. We applied the framework to benchmark problems as well as to a production-induced seismicity case. We investigated the effect of plastic failure on fault stability. We studied the impact of variation in the elastic moduli between reservoir and caprock and how this affects production-induced plasticity and slip. The main results are as follows:

1. The poroplastic reservoir exhibits larger vertical deformation and delayed slip than the poroelastic reservoir after the same amount of oil production because of plastic yielding.
2. Plastic dissipation releases a part of the mechanical energy generated by production-induced stresses. This reduces the energy available for seismic/aseismic slip and results in a delayed slip and a smaller magnitude slip event.
3. Reservoirs with smaller elastic moduli have a smaller pressure depletion for the same amount of production.
4. For the same amount of pressure drop, when the reservoir rock has smaller elastic moduli than those of the caprock, the vertical displacement is larger and plastic failure and fault slip begin earlier. When the caprock moduli are smaller than those of the reservoir, the vertical displacement is larger on the reservoir top surface and smaller on the ground surface (masking effect of the caprock). A higher pressure drop is required to activate plastic failure and fault slip in this case.

CRediT authorship contribution statement

Birendra Jha conceptualized and designed the study with Xiaoxi Zhao's input. Xiaoxi Zhao conducted modeling and simulations under Birendra Jha's supervision. Xiaoxi Zhao and Birendra Jha analyzed the results and wrote the paper.

Declaration of competing interest

The authors declare that they have no known competing financial interests or personal relationships that could have appeared to influence the work reported in this paper.

Acknowledgement

The support of the United States Department of Energy, National Energy Technology Laboratory through NETL-Penn State University Coalition for Fossil Energy Research (UCFER, contract DE-FE0026825) and the support of the American Chemical Society Petroleum Research Fund (58769-DNI9) are gratefully acknowledged.

Appendix A

Algorithmic Tangent Operator

Below, we derive the expression for the tangent operator, $\mathbf{D}^{n+1}$.

Large displacement/rotation–large strain The tangent modulus is [50]

$$\mathbf{D}^{n+1} = \frac{\partial \overset{\bullet}{\boldsymbol{\tau}}{}^{\prime,n+1}}{\partial \boldsymbol{d}^{n+1}} = \sum_{i=1}^{3}\sum_{j=1}^{3} \frac{\partial \tau_i'}{\partial \epsilon_j^{e,tr}} \boldsymbol{m}^i \otimes \boldsymbol{m}^j + \sum_{i=1}^{3}\sum_{j\neq i} \left(\frac{\tau_j' - \tau_i'}{\theta_j^{e,tr} - \theta_i^{e,tr}} \right) \left(\theta_j^{e,tr} \boldsymbol{m}^{i,j} \otimes \boldsymbol{m}^{i,j} + \theta_i^{e,tr} \boldsymbol{m}^{i,j} \otimes \boldsymbol{m}^{j,i} \right) \tag{71}$$

where $\boldsymbol{m}^i = \boldsymbol{n}^i \otimes \boldsymbol{n}^i$, $\boldsymbol{m}^{i,j} = \boldsymbol{n}^i \otimes \boldsymbol{n}^j$, and $\boldsymbol{n}^i$ are the eigenvectors of $\boldsymbol{\tau}^{\prime,n+1}$.

Large displacement/rotation–small strain We combine Eqs. (61) to obtain

$$\boldsymbol{dS}' = 2G\left(\boldsymbol{de} - \boldsymbol{de}^{\mathrm{p}}\right) + K_{dr}\left(dE_v - d\varepsilon_v^{\mathrm{p}}\right)\mathbf{1} \tag{72}$$

The tangent modulus is then given by

$$\mathbf{D}^{n+1} = \frac{\partial \boldsymbol{S}^{\prime,n+1}}{\partial \boldsymbol{E}^{n+1}} = 2G\left(\frac{\partial \boldsymbol{de}}{\partial \boldsymbol{E}^{n+1}} - \frac{\partial (\boldsymbol{de}^{\mathrm{p}})}{\partial \boldsymbol{E}^{n+1}} \right) + K_{dr}\left(\frac{\partial (dE_v \mathbf{1})}{\partial \boldsymbol{E}^{n+1}} - \frac{\partial (d\varepsilon_v^{\mathrm{p}} \mathbf{1})}{\partial \boldsymbol{E}^{n+1}} \right) \tag{73}$$

Using $\boldsymbol{e} = \boldsymbol{E} - (1/3)E_v\mathbf{1}$ and Voigt notation for tensors

$$\frac{\partial \boldsymbol{de}}{\partial \boldsymbol{E}^{n+1}} = \frac{1}{3}\begin{bmatrix} 2 & -1 & -1 & 0 & 0 & 0 \\ -1 & 2 & -1 & 0 & 0 & 0 \\ -1 & -1 & 2 & 0 & 0 & 0 \\ 0 & 0 & 0 & 3 & 0 & 0 \\ 0 & 0 & 0 & 0 & 3 & 0 \\ 0 & 0 & 0 & 0 & 0 & 3 \end{bmatrix} \tag{74}$$

and

$$\frac{\partial (dE_v \mathbf{1})}{\partial \boldsymbol{E}^{n+1}} = \frac{1}{3}\mathbf{1} \tag{75}$$

From Eq. (69),

$$\frac{\partial \boldsymbol{de}^{\mathrm{p}}}{\partial \boldsymbol{E}^{n+1}} = \frac{1}{r^{n+1}}\left[\left(\boldsymbol{de} + \frac{\boldsymbol{s}^n}{2G}\right)\left(\frac{\partial d\lambda}{\partial \boldsymbol{E}^{n+1}} - \frac{d\lambda}{r^{n+1}}\frac{\partial r^{n+1}}{\partial \boldsymbol{E}^{n+1}}\right) + d\lambda \frac{\partial \boldsymbol{de}}{\partial \boldsymbol{E}^{n+1}}\right]. \tag{76}$$

The last derivative term appearing in Eq. (73) is given by

$$\frac{\partial (d\varepsilon_v^{\mathrm{p}} \mathbf{1})}{\partial \boldsymbol{E}^{n+1}} = \alpha_g \frac{\partial (d\lambda)}{\partial \boldsymbol{E}^{n+1}}, \tag{77}$$

where the derivative of the plastic multiplier can be calculated from Eq. (67) as

$$\frac{\partial (d\lambda)}{\partial \boldsymbol{E}^{n+1}} = \frac{1}{K_{dr}\alpha_f \alpha_g + G}\left(\frac{\alpha_f K_{dr}}{3}\mathbf{1} + G\frac{\partial r^{n+1}}{\partial \boldsymbol{E}^{n+1}}\right) \tag{78}$$

From the definition of r^2 as the right hand side of Eq. (65),

$$\begin{aligned} \frac{\partial r^{n+1}}{\partial \boldsymbol{E}^{n+1}} &= \frac{1}{2r^{n+1}}\frac{\partial (r^{n+1})^2}{\partial \boldsymbol{E}^{n+1}} \\ &= \frac{1}{r^{n+1}}\left(\frac{\partial \boldsymbol{de} : \boldsymbol{de}}{\partial \boldsymbol{E}^{n+1}} + \frac{1}{G}\frac{\partial \boldsymbol{s}^n : \boldsymbol{de}}{\partial \boldsymbol{E}^{n+1}}\right) \end{aligned} \tag{79}$$

The first derivative above is

$$\begin{aligned} \frac{\partial \boldsymbol{de} : \boldsymbol{de}}{\partial \boldsymbol{E}^{n+1}} &= \frac{\partial \boldsymbol{de} : \boldsymbol{de}}{\partial \boldsymbol{de}}\frac{\partial \boldsymbol{de}}{\partial \boldsymbol{E}^{n+1}} \\ &= 2\boldsymbol{de} : \frac{\partial \boldsymbol{de}}{\partial \boldsymbol{E}^{n+1}} = 2\boldsymbol{de}, \end{aligned} \tag{80}$$

where we used Eq. (74) and the relation $\boldsymbol{de}\mathbf{1} = 0$. The second derivative is

$$\frac{\partial \boldsymbol{s}^n : \boldsymbol{de}}{\partial \boldsymbol{E}^{n+1}} = \boldsymbol{T}^{n+1}, \tag{81}$$

where $T_i = s_i^n$ for $i = 1, 2, 3$ and $T_i = 2s_i^n$ for $i = 4, 5, 6$. Therefore,

$$\frac{\partial r^{n+1}}{\partial \boldsymbol{E}^{n+1}} = \frac{2\boldsymbol{de} + (\boldsymbol{T}^{n+1}/G)}{r^{n+1}} \tag{82}$$

Relation between the two sets of Drucker-Prager model parameters For the inscribed version of the model where the D-P yield surface touches the outer vertices of the M-C yield surface, we have

$$\alpha_f = \frac{2\sin\phi_f}{\sqrt{3}(3-\sin\phi_f)},\ \alpha_g = \frac{2\sin\phi_g}{\sqrt{3}(3-\sin\phi_g)},\ \gamma = \frac{6c\cos\phi_f^0}{\sqrt{3}(3-\sin\phi_f^0)}$$

where ϕ_f is the friction angle, ϕ_g is the dilatation angle, ϕ_f^0 is the initial friction angle, and c is the cohesion. ϕ_f and ϕ_g are functions of the hardening parameter h.

Appendix B. Supplementary material

Supplementary material related to this article can be found online at https://doi.org/10.1016/j.jcp.2021.110178.

References

[1] C.B. Raleigh, J.H. Healy, J.D. Bredehoeft, An experiment in earthquake control at Rangely, Colorado, Science 191 (1976) 1230–1237.
[2] R.F. Yerkes, R.O. Castle, Seismicity and faulting attributable to fluid extraction, Eng. Geol. 10 (1976) 151–167.
[3] P. Segall, Earthquakes triggered by fluid extraction, Geology 17 (1989) 942–946.
[4] P. Segall, Stress and subsidence resulting from subsurface fluid withdrawal in the epicentral region of the 1983 Coalinga earthquake, J. Geophys. Res. 90 (1985) 6801–6816.
[5] P. Segall, J.-R. Grasso, A. Mossop, Poroelastic stressing and induced seismicity near the Lacq gas field, J. Geophys. Res. 99 (1994) 15423–15438, https://doi.org/10.1029/94JB00989.
[6] S.E. Minkoff, C.M. Stone, S. Bryant, M. Peszynska, M.F. Wheeler, Coupled fluid flow and geomechanical deformation modeling, J. Pet. Sci. Eng. 38 (2003) 37–56.
[7] A.W. Chan, M.D. Zoback, The role of hydrocarbon production on land subsidence and fault reactivation in the Louisiana coastal zone, J. Coast. Res. 23 (2007) 771–786, https://doi.org/10.1306/11111313009.
[8] R. Juanes, B. Jha, B.H. Hager, J.H. Shaw, A. Plesch, L. Astiz, J.H. Dieterich, C. Frohlich, Were the May 2012 Emilia-Romagna earthquakes induced? A coupled flow-geomechanics modeling assessment, Geophys. Res. Lett. (2016), https://doi.org/10.1002/2016GL069284.
[9] P.F. Sanz, S.P. Lele, K.H. Searles, S.-Y. Hsu, J.L. Garzon, J.A. Burdette, W.E. Kline, B.A. Dale, P.D. Hector, Geomechanical analysis to evaluate production-induced fault reactivation at groningen gas field, in: Soc. Pet. Eng., 2015, SPE-174942-MS.
[10] K.v. Thienen-Visser, P.A. Fokker, The future of subsidence modelling: compaction and subsidence due to gas depletion of the groningen gas field in the Netherlands, Netherlands J. Geosci. 96 (5) (2017) s105–s116.
[11] P.J. Gonzalez, K.F. Tiampo, M. Palano, F. Cannavo, J. Fernandez, The 2011 Lorca earthquake slip distribution controlled by groundwater crustal unloading, Nat. Geosci. 5 (2012) 821–825.
[12] K.M. Keranen, H.M. Savage, G.A. Abers, E.S. Cochran, Potentially induced earthquakes in Oklahoma, USA: links between wastewater injection and the 2011 M_w 5.7 earthquake sequence, Geology 41 (2013) 699–702.
[13] S. Horton, Disposal of hydrofracking waste fluid by injection into subsurface aquifers triggers earthquake swarm in central Arkansas with potential for damaging earthquake, Seismol. Res. Lett. 83 (2012) 250–260.
[14] S.M. Hosseini, T.H.W. Goebel, B. Jha, F. Aminzadeh, A probabilistic approach to injection-induced seismicity assessment in the presence and absence of flow boundaries, Geophys. Res. Lett. 45 (2018) 8182–8189, https://doi.org/10.1029/2018GL077552.
[15] J.P. Morris, Y. Hao, W. Foxall, W. McNab, A study of injection-induced mechanical deformation at the In Salah CO_2 storage project, Int. J. Greenh. Gas Control 5 (2) (2011) 270–280.
[16] B. Jha, R. Juanes, Coupled multiphase flow and poromechanics: a computational model of pore pressure effects on fault slip and earthquake triggering, Water Resour. Res. 50 (5) (2014) 3776–3808, https://doi.org/10.1002/2013WR015175.
[17] X. Zhao, B. Jha, Role of well operations and multiphase geomechanics in controlling fault stability during CO_2 storage and enhanced oil recovery, J. Geophys. Res. 124 (2019), https://doi.org/10.1029/2019JB017298.
[18] K. Deng, Y. Liu, R.M. Harrington, Poroelastic stress triggering of the December 2013 Crooked Lake, Alberta, induced seismicity sequence, Geophys. Res. Lett. 43 (2016) 8482–8491.
[19] V. Maury, J.M. Piau, G. Halle, Subsidence induced by water injection in water sensitive reservoir rocks: the example of ekofisk, in: European Petroleum Conference, Milan, Italy, 1996, SPE 36890.
[20] K. Bennett, L. Berla, W. Nix, R. Borja, Instrumented nanoindentation and 3d mechanistic modeling of a shale at multiple scales, Acta Geotech. 10 (2015) 1–14.
[21] R.O. Davis, A.P.S. Selvadurai, Plasticity and Geomechanics, Cambridge University Press, New York, 2002.
[22] C.H. Scholz, Microfracturing and the inelastic deformation of rock in compression, J. Geophys. Res. 73 (1968) 1417–1432.
[23] R.L. Ireland, J.F. Poland, F.S. Riley, Land subsidence in the San Joaquin Valley, California, as of 1980, U.S. Geol. Surv. Prof. Pap. 93 (1984), 437–I.
[24] D.L. Galloway, F.S. Riley, San Joaquin Valley, California - largest human alteration of the Earth's surface, in: D.L. Galloway, D.R. Jones, S.E. Ingebritsen (Eds.), Land Subsidence in the United States, U.S. Geological Survey Circular, 1999, pp. 23–34.
[25] D.R. Allen, Physical changes of reservoir properties caused by subsidence and repressurizing operations, Wilmington field, California, J. Pet. Technol. 20 (1968) 23–29.
[26] D.R. Allen, M.N. Mayuga, The Mechanics of Compaction and Rebound, Wilmington Oilfield, Long Beach, CA, USA, Land Subsidence, vol. 89, IASH-UNESCO, Tokyo, 1969, pp. 410–413.
[27] L.Y. Chin, L.K. Thomas, Fully-coupled geomechanics and fluid-flow analysis of wells with stress-dependent permeability, in: SPE International Conference and Exhibition, Beijing, China, 1998, SPE 48857.
[28] H. Sone, M.D. Zoback, Visco-plastic properties of shale gas reservoir rocks, in: 45th US Rock Mechanics Geomechanics Symposium, no. ARMA 11-417, San Francisco, CA, 2011.
[29] C. Chang, E. Mallman, M.D. Zoback, Time-dependent subsidence associated with drainage-induced compaction in Gulf of Mexico shales bounding a severely depleted gas reservoir, Am. Assoc. Pet. Geol. Bull. 98 (2014) 1145–1159, https://doi.org/10.1306/11111313009.
[30] X.Y. Gu, Q.Q. Ran, Land subsidence, in: Proc. 6th Int. Symposium on Land Subsidence, vol. 11, 2000, pp. 355–365.
[31] M.C.F.G. Bell, J.C. Cripps, A review of the engineering behaviour of soils and rocks with respect to groundwater, Geochem. Soc. Lond. Eng. Geol. Spec. Publ. 3 (1986) 1–23.
[32] X.-Q. Shi, Y.-Q. Xue, S.-J. Ye, J.-C. Wu, Y. Zhang, J. Yu, Characterization of land subsidence induced by groundwater withdrawals in Su-Xi-Chang area, China, Environ. Geol. 52 (2007) 27, https://doi.org/10.1007/s00254-006-0446-3.
[33] J.T. Fredrich, J.G. Arguello, G.L. Deitrick, E.P. de Rouffignac, Geomechanical modeling of reservoir compaction, surface subsidence, and casing damage at the Belridge diatomite field, SPE Reserv. Eval. Eng. 3 (2000) 348–359.
[34] C.H. Scholz, The Mechanics of Earthquakes and Faulting, 2nd edition, Cambridge University Press, Cambridge, UK, 2002.
[35] S.J. Bourne, S.J. Oates, Extreme threshold failures within a heterogeneous elastic thin sheet and the spatial-temporal development of induced seismicity within the groningen gas field, J. Geophys. Res. 122 (2017) 10,299–10,320.
[36] F. Armero, J.C. Simo, A priori stability estimates and unconditionally stable product formula algorithms for nonlinear coupled thermoplasticity, Int. J. Plast. 9 (1993) 749–782.
[37] R.I. Borja, E. Alarcon, A mathematical framework for finite strain elastoplastic consolidation part 1: balance laws, variational formulation, and linearization, Comput. Methods Appl. Mech. Eng. 122 (1995) 145–171.
[38] F. Armero, Formulation and finite element implementation of a multiplicative model of coupled poro-plasticity at finite strains under fully saturated conditions, Comput. Methods Appl. Mech. Eng. 171 (1999) 205–241.
[39] L. Sanavia, B.A. Schrefler, P. Steinmann, A formulation for an unsaturated porous medium undergoing large inelastic strains, Comput. Mech. 28 (2002) 137–151, https://doi.org/10.1007/s00466-001-0277-8.
[40] R.I. Borja, Cam-Clay plasticity. Part V: a mathematical framework for three-phase deformation and strain localization analyses of partially saturated porous media, Comput. Methods Appl. Mech. Eng. 193 (2004) 5301–5338.

[41] X. Li, Z. Liu, R.W. Lewis, Mixed finite element method for coupled thermo-hydro-mechanical process in poro-elastic-plastic media at large strains, Int. J. Numer. Methods Eng. 64 (5) (2005) 667–708.
[42] A. Benallal, A.S. Botta, W.S. Venturini, Consolidation of elastic–plastic saturated porous media by the boundary element method, Comput. Methods Appl. Mech. Eng. 197 (2008) 4626–4644.
[43] R.I. Borja, C. Tamagnini, E. Alarcón, Elastoplastic consolidation at finite strain part 2: finite element implementation and numerical examples, Comput. Methods Appl. Mech. Eng. 159 (1998) 103–122.
[44] C. Callari, F. Armero, Analysis and numerical simulation of strong discontinuities in finite strain poroplasticity, Comput. Methods Appl. Mech. Eng. 193 (2004) 2941–2986.
[45] W. Sun, J.T. Ostien, A.G. Salinger, A stabilized assumed deformation gradient finite element formulation for strongly coupled poromechanical simulations at finite strain, Int. J. Numer. Anal. Methods Geomech. 37 (2013) 2755–2788.
[46] S. Teichtmeister, S. Mauthe, C. Miehe, Aspects of finite element formulations for the coupled problem of poroelasticity based on a canonical minimization principle, Comput. Mech. 64 (3) (2019) 685–716.
[47] K. Wang, W. Sun, An updated Lagrangian LBM–DEM–FEM coupling model for dual-permeability fissured porous media with embedded discontinuities, Comput. Methods Appl. Mech. Eng. 344 (2019) 276–305.
[48] O. Coussy, Poromechanics, John Wiley and Sons, Chichester, England, 2004.
[49] J.C. Simo, Algorithms for static and dynamic multiplicative plasticity that preserve the classical return mapping schemes of the infinitesimal theory, Comput. Methods Appl. Mech. Eng. 99 (1992) 61–112.
[50] R.I. Borja, Finite element simulation of strain localization with large deformation: capturing strong discontinuity using a Petrov–Galerkin multiscale formulation, Comput. Methods Appl. Mech. Eng. 191 (2002) 2949–2978.
[51] A. McGarr, On relating apparent stress to the stress causing earthquake fault slip, J. Geophys. Res. 104 (1999) 3003–3011.
[52] T.C. Hanks, H. Kanamori, A moment magnitude scale, J. Geophys. Res. 84 (1979) 2348–2350.
[53] K.J. Bathe, Finite Element Procedures, Prentice Hall, New Jersey, 1995.
[54] R.I. Borja, On the mechanical energy and effective stress in saturated and unsaturated porous continua, Int. J. Solids Struct. 43 (2006) 1764–1786.
[55] A. Bubshait, B. Jha, Coupled poromechanics-damage mechanics modeling of fracturing during injection in brittle rocks, Int. J. Numer. Methods Eng. (2019) 1–21, https://doi.org/10.1002/nme.6208.
[56] Y. Zhao, R.I. Borja, A continuum framework for coupled solid deformation–fluid flow through anisotropic elastoplastic porous media, Comput. Methods Appl. Mech. Eng. 369 (2020) 113–225, https://doi.org/10.1016/j.cma.2020.113225.
[57] Z. Yang, R. Juanes, Two sides of a fault: grain-scale analysis of pore pressure control on fault slip, Phys. Rev. E 97 (2018) 022906, https://doi.org/10.1103/PhysRevE.97.022906.
[58] O. Coussy, Mechanics of Porous Continua, John Wiley and Sons, Chichester, England, 1995.
[59] R.W. Lewis, B.A. Schrefler, The Finite Element Method in the Static and Dynamic Deformation and Consolidation of Porous Media, 2nd edition, Wiley, Chichester, England, 1998.
[60] J.C. Simo, T.J.R. Hughes, Computational Inelasticity, Springer, New York, 1998.
[61] R.I. Borja, Plasticity Modeling & Computation, Springer, New York, 2013.
[62] S. Balay, S. Abhyankar, M.F. Adams, J. Brown, P. Brune, K. Buschelman, L. Dalcin, A. Dener, V. Eijkhout, W.D. Gropp, D. Karpeyev, D. Kaushik, M.G. Knepley, D.A. May, L.C. McInnes, R.T. Mills, T. Munson, K. Rupp, P. Sanan, B.F. Smith, S. Zampini, H. Zhang, PETSc web page, https://www.mcs.anl.gov/petsc, 2019.
[63] B.T. Aagaard, M.G. Knepley, C.A. Williams, A domain decomposition approach to implementing fault slip in finite-element models of quasi-static and dynamic crustal deformation, J. Geophys. Res. 118 (2013) 3059–3079.
[64] K. Nikitin, K. Terekhov, Y. Vassilevski, A monotone nonlinear finite volume method for diffusion equations and multiphase flows, Comput. Geosci. 18 (2014) 311–324, https://doi.org/10.1007/s10596-013-9387-6.
[65] B. Aagaard, S. Kientz, M. Knepley, L. Strand, C. Williams, PyLith User Manual, Version 1.8.0, Computational Infrastructure for Geodynamics, University of California, Davis, 2012, geodynamics.org/cig/software/pylith/pylith_manual-1.8.pdf.
[66] H.F. Wang, Theory of Linear Poroelasticity with Applications to Geomechanics and Hydrogeology, Princeton University Press, 2000.
[67] J.P. Carter, J.R. Booker, J.C. Small, An improved method for calculating water influx, Int. J. Numer. Anal. Methods Geomech. 3 (1979) 107–129.
[68] C.H. Scholz, Mechanics of faulting, Annu. Rev. Earth Planet. Sci. 17 (1989) 309–334.
[69] S. Ide, M. Takeo, Determination of constitutive relations of fault slip based on seismic wave analysis, J. Geophys. Res. 102 (1997) 27379–27391.
[70] K.B. Olsen, R. Madariaga, R.J. Archuleta, Three-dimensional dynamic simulation of the 1992 Landers earthquake, Science 278 (1997) 834–838.
[71] T. Mikumo, K.B. Olsen, E. Fukuyama, Y. Yagi, Stress-breakdown time and slip-weakening distance inferred from slip-velocity functions on earthquake faults, Bull. Seismol. Soc. Am. 93 (2003) 264–282.
[72] E. Sarris, P. Papanastasiou, Numerical modeling of fluid–driven fractures in cohesive poroelastoplastic continuum, Int. J. Numer. Anal. Methods Geomech. 37 (12) (2013) 1822–1846.
[73] K. Aziz, A. Settari, Petroleum Reservoir Simulation, Elsevier, London, 1979.